

ORIGINAL ARTICLE

Effects of Different Orientation Angle, Size, Surface Roughness, and Heat Curing on Mechanical Behavior of 3D Printed Cement Mortar With/Without Glass Fiber in Powder-Based 3DP

Pshtiwan Shakor,¹ Shami Nejadi,¹ Gavin Paul,² and Nadarajah Gowripalan²

Abstract

Powder-based (inkjet) three-dimensional printing (3DP) technology presents great promise in the construction industry. The capacity to build complex geometries is one of the most appealing features of the process without formwork. This article focuses on the vital aspect of using a modified powder (CP) instead of commercial powder (ZP 151). It also discusses the effects of the size of specimens and the curing process of 3DP specimens. This article presents not only the improved mechanical properties of the mortar that are revealed through a heat-curing procedure but also the properties of the reinforced mortar with chopped glass fibers. Experiments are conducted on cubic printed mortar specimens and cured in an oven at different temperature regimes. Tests show that 80°C is the optimum heat-curing temperature to attain the highest compressive and flexural strength of the specimens. The orientation angle has a significant effect on the mechanical behavior of printed specimens. Therefore, specimens are prepared by printing at different orientation angles to compare the mechanical properties of common construction materials. Powder-based 3DP has three planes (*XY*, *XZ*, and *YZ*) along which a load can be applied to the specimen. The mechanical strength in each direction across each plane is different, making it an anisotropic material. For CP specimens, the highest compressive strength was obtained using a 0° rotation in the printing orientation of the *XY* plane. For shear strength, a 45° orientation gave the optimum result, while for tensile and flexural strength, a 0° orientation provided the highest values. The optimum strength for ZP 151 specimens in compression, shear, tension, and bending was obtained by printing with orientation angles of 0°, 30°, 0°, and 0°, respectively. Finally, laser scanning of the printed specimens has been conducted so the surface roughness profiles for the 3DP specimens of ZP 151 and CP can be compared and presented.

Keywords: powder-based 3DP, printing orientations, glass fiber, mechanical strength, surface roughness

Highlights

- Incorporation of chopped strand glass fiber in cement mortar fitted in a powder-based three-dimensional printer.
- Comparison of compressive strength of the small printed cube (20×20×20) mm³ and the large printed cube (50×50×50) mm³ with/without chopped glass fiber.
- Surface roughness of the commercial powders and specimens compared with modified powders and specimens.
- Determining the effect of orientation angle in three-dimensional printing on the mechanical properties of cementitious materials.
- Compressive, shear, tensile, and flexural strength have been conducted to determine the mechanical behavior of cementitious materials.
- The most suitable printing orientations and angles exhibiting the highest mechanical strength have been discovered.

¹School of Civil and Environmental Engineering, University of Technology Sydney, Sydney, Australia.

²School of Mechanical and Mechatronic Engineering, University of Technology Sydney, NSW, Australia.

Introduction

GENERALLY, STRUCTURAL MEMBERS in civil engineering are cast *in situ* or they are constructed using precast procedures. Concrete and masonry are traditionally considered to be the most appropriate material for use in structural members.¹ However, there is an increasing need for speed, quality, and bespoke and adaptable designs in the construction industry. Therefore, the procedures for constructing structural members should be reconsidered and advanced² to take advantage of the recent developments in rapid prototyping.³

Additive manufacturing (AM) is known as “a process of joining materials to make objects from 3D model data, usually layer upon layer, as opposed to subtractive manufacturing methodologies.”^{4,5} AM has been shown in certain cases to increase the production rate, while providing freedom in fabrication and reducing the cost of formwork by 35–60%.^{6,7}

Powder bed printing (binder/inkjet printing) has been used in numerous applications for medical and biomedical purposes.⁸ The key mechanism of this technique is to allow a drop of binder (water) to fall through a certain height on to the bedded dry powder. The particular binder is used, and has a major influence on the resolution, dimensional accuracy, and surface finish of the printed parts.^{9,10} The printer that is used in this study is a commercial printer, ProJet CJP 360, developed by Z-corp. However, all types of powder-based three-dimensional (3D) printers adopt a similar process. The ProJet CJP 360 has a maximum resolution of 300×450 dots per inch (DPI).¹¹

Size and scaling related challenges in three-dimensional printing

The size of the specimens is a key challenge that must be overcome to allow them to be used in concrete construction and civil engineering applications. In earlier research, cast-in-place cubic mortar specimens in varying sizes have been studied, and the authors observed that larger specimens exhibit a reduced compressive strength of the mortar.^{12,13} Therefore, this study is proposing to discover the real properties of the three-dimensional printing (3DP) specimens and the mechanical behavior of the structure as the size is increased. It is well understood that conventional mortar has isotropic properties.¹⁴ However, generally, 3DP structures are printed with materials that have anisotropic properties (plastics, ceramic, cementitious, and composite materials).^{15–17} Therefore, there is still a need to investigate 3D printed mortar, in particular, the size effect and physical properties of the 3D printed cementitious parts.

Surface roughness

This research also investigates the surface roughness of the powder materials and printed parts. A study has previously been conducted on cast-in-place mortar prisms with different surface roughnesses reinforced with a 3DP polymer.¹⁸ The study found that the smooth surface regions of the reinforced fiber bar could not be held by the mortar particles, whereas the areas with a rough surface had improved adhesion since the bar was also a 3D printed part. The surface roughness of printed objects has been found to be directly related to the size of the powder particles and the spread of powder bed in

the build chamber.¹⁹ Another factor that affects the resolution is the flowability of the powder and the spreading of the powder particles in the build chamber (build bin) by the roller.^{19,20} Therefore, there is a significant need to investigate the surface roughness of cement mortar powder-based 3DP at different stages of printing. Besides, this study showed improvement in the surface roughness of materials, while adding fiber in the matrix; however, earlier studies proved that flexural strength could be improved by adding glass fiber with more than 1780% to non-reinforced concrete.²¹

Effect of heat curing

Concrete commonly provides enough fire resistance for most normal applications. Nevertheless, the strength of concrete decreases at high temperatures due to chemical and physical changes.²² At high temperatures (i.e., above 400°C), spalling of conventional concrete occurs, resulting in a rapid layer-by-layer loss of concrete surface and, most significantly, the possibility of exposing the reinforcement bars in the concrete.²³ This has motivated significant research efforts on the application of different types of cement at different temperatures so as to find the optimum strength and optimum heat resistance of concrete. Research is also being conducted into the use of fiber reinforcement to enable concrete and mortar to exhibit improved mechanical behaviors.²⁴ There are only a few studies specifically related to fiber reinforced gypsum and mortar for 3DP technology. Feng *et al.*²⁵ used fiber reinforced polymer (FRP) sheeting to reinforce the gypsum printed parts. Christ *et al.*²⁶ used chopped glass fiber with a length of 1–2 mm to prepare a gypsum reinforced scaffold. Farina *et al.*²⁷ utilized the 3D printed polymeric and metallic fibers embedded in the cast-in-place mortar to compare reinforced mortar specimens with two types of 3D printed rebar. Panda *et al.*²⁸ used an extrusion methodology to print geopolymers using glass fiber lengths of 3, 6, and 8 mm. The literature suggests that the use of glass fiber as reinforcement in 3D printed components is more feasible than using other types of fiber. Generally, E-glass fibers are prone to alkali attack of the cement matrix. In this study, E6-glass fiber, which has suitable resistance to alkali attack, is used. Glass fiber with a length of 6 mm was used to print mortar specimens with the current powder-based 3DP technique.

Orientation angle

In powder-based 3DP, there are many limitations while printing objects, for example,²⁹ discussed several limitations related to the binder selection, powder reactions, post-processing bed manipulations, and de-powdering. One of the major limitations in 3DP is the orientation angle, which has been discussed in earlier studies for polymers.³⁰ The orientation angle is the rotation angle of the printed object in the plane that has a restricted boundary in the 3DP (Fig. 1). Similar to Dizon *et al.*¹³ study, Letcher and Waytashek³¹ worked on PLA materials in three orientation angles. They observed that the 45° raster orientation specimens had the strongest mechanical properties. The aforementioned limitations were not evident in the powder-based 3DP mortar and gypsum. Therefore, it is important to investigate the effect of orientation angle on the printed object, while concurrently clarifying the mechanical properties and the behavior of the

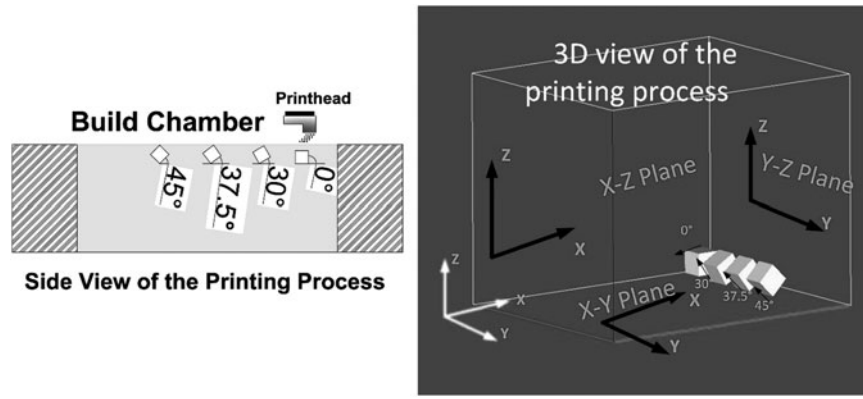


FIG. 1. Schematic illustration of the orientation angle for the powder-based 3D printed object. 3D, three dimensional.

modified powder (CP) in comparison to the recommended powder (ZP 151). However, in this study, there is no change in the orientation of fiber. Fiber is embedded and printed mostly parallel to Y-axis in the build chamber. However, there are limited studies on fiber reinforced powder-based 3DP, such as Coelho *et al.*³² found that the fiber in powder-based 3DP of gypsum oriented in Y-axis and increased strength about 60% in that direction. This is also proved experimentally and theoretically in the study of the author that XY plane provides a higher strength.³³

The objective of this study is to experimentally scrutinize the performance of 3DP mortar printed by the powder-based technique under the conditions of (1) high temperatures and (2) the incorporation of chopped filament fiber to reinforce the printed specimens. This article investigates the effects of specimen size, and then evaluates the compressive and flexural strengths of the 3DP mortar at a variety of curing temperatures. The performance is examined when the parts are printed using different orientation angles. Finally, the maximum compressive, shear, tensile, and flexural strengths are reported for both CP and ZP 151.

Materials and Methods

Materials

Powder preparation. The modified powder (CP) consists of ordinary Portland cement (OPC), calcium aluminate cement (CAC), and fine sand. This is used instead of commercial powder (ZP151) due to affordability of the materials, higher strength, and durability. CP is used based on ZP 151 whose major chemical composition is calcium sulfate

hemihydrate ($\text{CaSO}_4 \cdot 0.5\text{H}_2\text{O}$; 80–90%) and is produced by 3D Systems.³⁴ The particle sizes have been engineered to be as close as possible to the commercial material (ZP 151). The cumulative distribution and particle size of ZP 151 and the CP are presented in the previous study.³⁵

The modified powder that is used for powder-based 3DP in this research contains 67.8% of CAC using a ranging sieve of 75–150 μm , 32.2% of OPC, and 5% of fine sand as a percentage of total weight. The chemical composition of the cementitious materials is shown in Table 1.

The surface area and bulk density of each of the powders have been established in a previous study.³⁵ The bulk density of ZP 151 has been found to be greater than the bulk density of CP, which means that ZP 151 has more densely packed powder than the CP. Therefore, the porosity was higher in the CP specimens than in ZP 151. The results of this study were consistent with those of Zhang *et al.*,³⁶ who found that increasing the bulk density of powder significantly decreased porosity in the powder.

Powder mixing. After selecting the type of materials and their mix proportions, the materials were blended homogeneously. The modified powder was thoroughly mixed using a Hobart mixer at a speed of 1450 revolutions per minute.

The homogeneity and consistency of the powder are significant factors that must be controlled when in pursuit of superior surface roughness and strength results. The speed of the mixer and the blending time are the main contributors to the homogeneity of the powder, and thus to the production of better quality 3DP objects.³⁷

TABLE 1. PERCENTAGES OF THE MAIN CHEMICAL CONSTITUENTS OF CEMENT MORTAR (CP) AND ZP 151

| Chemical composition | CP | | | ZP 151 Gypsum plaster |
|--|--------------------------|--------------------------|--------------|--------------------------|
| | Ordinary portland cement | Calcium aluminate cement | Fine sand | |
| Silica (SiO_2) | 17–25% | ≤ 6.0 | $\sim 100\%$ | — |
| Lime (CaO) | 60–67% | ≤ 39.8 | — | — |
| Alumina (Al_2O_3) | 3–8% | > 37.0 | — | — |
| Iron oxide (Fe_2O_3) | 0.5–6% | ≤ 18.5 | — | — |
| Magnesia (MgO) | 0.1–4% | ~ 1 | — | — |
| Calcium sulfate hemihydrate ($\text{CaSO}_4 \cdot 0.5\text{H}_2\text{O}$) | — | — | — | 80–90% |
| Vinyl polymer | — | — | — | 10–20% |

TABLE 2. DETAILED NUMBER AND DIMENSION OF SPECIMENS (GROUP 1)

| <i>Specimen description</i> | <i>CAD dimensions (mm)</i> | <i>No. of specimens</i> | <i>Printed plane</i> |
|-----------------------------|----------------------------|-------------------------|-------------------------|
| Plain cube | 20×20×20 | 54 | XY, ^a XZ, YZ |
| Plain cube | 50×50×50 | 54 | XY, XZ, YZ |
| Plain prism | 160×40×40 | 18 | XZ |
| Fiber reinforced cube | 50×50×50 | 54 | XY, XZ, YZ |
| Fiber reinforced prism | 160×40×40 | 18 | XZ |

^aParallel to the printhead, see Figure 4.

Binder (Zb 63). The inkjet binder is made of liquid water and humectant.³⁸ This agent binder is produced in a formulation that easily flows through the printhead nozzles with a surface tension of 0.00045 N/cm and a viscosity of 0.0135 g/cm·s.³⁹ A complete description of the binder and test preparation has been presented in the author’s earlier work.^{35,39} Binder dosage and resolution section gives details on the binder dosage and resolution.

Methods

Specimen preparation. CP specimens with dimensions of (20×20×20) mm³ and (50×50×50) mm³ were arranged for a compressive strength test. For the flexural strength tests, specimens with dimensions of (160×40×40) mm³ were prepared. As shown in Table 2, three specimens were prepared for each test.

Figure 1 provides all the details of the planes (XY, XZ, and YZ) and the applied loads on those planes. The E6-glass fiber was used in the printing fabrication and the physical properties of these fibers are shown in Table 3.

Figure 2 displays the green part for (Fig. 2a) a 3DP mortar prism and (Fig. 2b) a cube. The green part is the name given to the fabricated part after printing and removal from the build chamber of the printer, before commencing any postprocessing procedures such as curing. All specimens were cured under two different regimes: (1) tap water curing only and (2) heat curing, followed by water curing and then heat curing again.

The ZP 151 powder has been directly placed into the 3DP (ProJet 360). However, the modified mix was prepared by a 20L Hobart mixer. The mixing procedure has been conducted in a dry mix state. The prepared mix powder was then placed into the powder-based 3DP to print the mortar specimens. The thickness of each printed layer was 0.1 mm and the layer-by-layer printing procedure is continued until the structure is complete. Different orientation angles have been used to print the specimens. Figure 3 schematically shows the specimens with different orientation angles for the printed objects. For each orientation angle, each geometry type, and each powder type, three specimens have been prepared for testing.

Table 4 shows the types of mechanical tests, the number of specimens, the dimensions of the specimens, and the CAD drawing of the print parameters.

Postprocessing of specimen. After a specimen is printed, it is cured in two different ways (these curing methodologies are more common for the construction industry). Some specimens were cured in tap water only. The rest of the specimens were cured with one of the following (heat, water immersion, and heat) regimes that involved (1) curing in the oven for 3 h; (2) curing for 28 days in tap water; and (3) then drying in the oven for 3 h. For different specimens, the curing/drying temperature was chosen to be somewhere from 40°C to 100°C, as follows: (3 h at 40°C, 28 days in water, and 3 h at 40°C), (3 h at 60°C, 28 days in water, and 3 h at 60°C), (3 h at 80°C, 28 days in water, and 3 h at 80°C), (3 h at 90°C, 28 days in water, and 3 h at 90°C), and (3 h at 100°C, 28 days in water, and 3 h at 100°C). This same basic postprocessing sequence was used for all specimens, but at various temperatures to investigate and find for the optimized maximum compressive strength of the printed specimen.

Experimental Program

Experimental for specimens in group 1

Small and large cubic specimens were subjected to the compressive strength test and the prism specimens were subjected to the flexural strength test.

The compressive strength test was performed for the 3DP specimens according to the ASTM standard.⁴⁰ A total of 162 specimens were printed and tested, including 3 specimens for each plane, 3 specimens for each curing process, and 3 specimens with the presence/absence of glass fiber. The rate of loading in the compressive strength test was fixed at 0.833 kN/s. The two different sizes (20×20×20) mm³ and (50×50×50) mm³ were designated to evaluate the size effect and the heat temperature curing of the printed specimens.

The specimens were tested for flexural strength in a three-point bending test according to the ASTM standard.⁴¹ A total of 36 specimens were printed and tested, including 3 specimens prepared for each plane, 3 specimens for each of the curing media processes, and 3 specimens with the presence/absence of glass fiber. The rate of loading in this test was 426 N/min.

Surface roughness test. The surface roughness profile and image of the surface of the printed specimen were taken

TABLE 3. PHYSICAL PROPERTIES OF CHOPPED E6-GLASS FIBER FILAMENT

| <i>Fiber type</i> | <i>Length (mm)</i> | <i>Filament diameter (μm)</i> | <i>Specific gravity (g/cm³)</i> | <i>Tensile strength (MPa)</i> | <i>Tensile modulus (GPa)</i> | <i>Expansion coefficient (10⁻⁶ K⁻¹)</i> |
|-------------------------|--------------------|-------------------------------|--|-------------------------------|------------------------------|---|
| E6-Glass fiber (Trojan) | 6±1 | 13±1 | 2.62–2.63 | 2500–2700 | 81 | 6 |

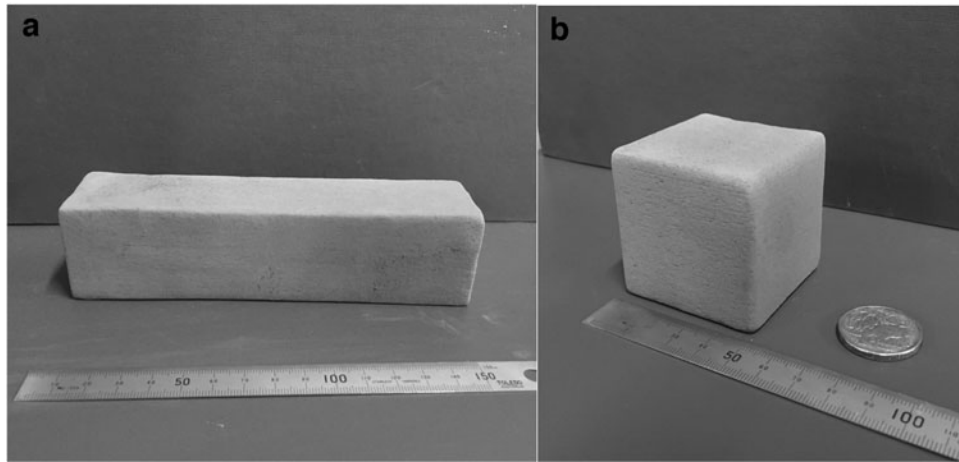


FIG. 2. (a) Green part of 3DP cement mortar prism, (b) green part of 3DP cement mortar cube. 3DP, three-dimensional printing.

using a 3D microscope scanner (Olympus LEXT OLS5000). The photos were taken at appropriate magnification levels to show the fiber orientation in the build chamber of the printer and to display the fiber in the printed CP specimen. Therefore, the magnification level of (20×L) and a working distance of 6.5 mm were used.

Glass fiber orientation. This study also examined the fiber orientation in the build chamber of the printer and the printed specimens (Fig. 4). It was shown from Figure 4 that the orientation of most bedded fiber filaments was in the Y-direction, with only a few fiber filaments bedded in the X-direction. This phenomenon was also observed after removing the specimen from the build chamber by observing the other sides of the specimens.

As shown in Figure 4, to see the embedding of the fibers in the cement mortar powder, the build chamber of the printer was removed and examined under the 3D laser microscope (LEXT OLS5000). In this way, it was possible to identify the location and bedding of the individual filaments, or occa-

sionally, a bundle of filaments clumped together at other places (Fig. 5). It was clear that the Y-axis had more fibers bedded on the powder. Knowing the fiber orientation in the printing process is significant because it affects the mechanical strength of the printed objects. This study was aimed at determining the best plane for printing, which maximizes the mechanical strength.

Binder solution. Binder is a liquid solution that contains mainly water and a small portion of humectant. The binder liquid acts as an agent to activate the main powder, which in this case are the cementitious materials. This liquid solution has a major impact on the strength of the printed parts because the printing process is different from conventional casting. In 3DP, a small amount of liquid is carefully dropped on a specific area, while in the conventional casting method, water is poured into and mixed with all the powder. This difference directly affects the mechanical behavior of the materials. The details are presented and discussed in the Results and Discussion section.

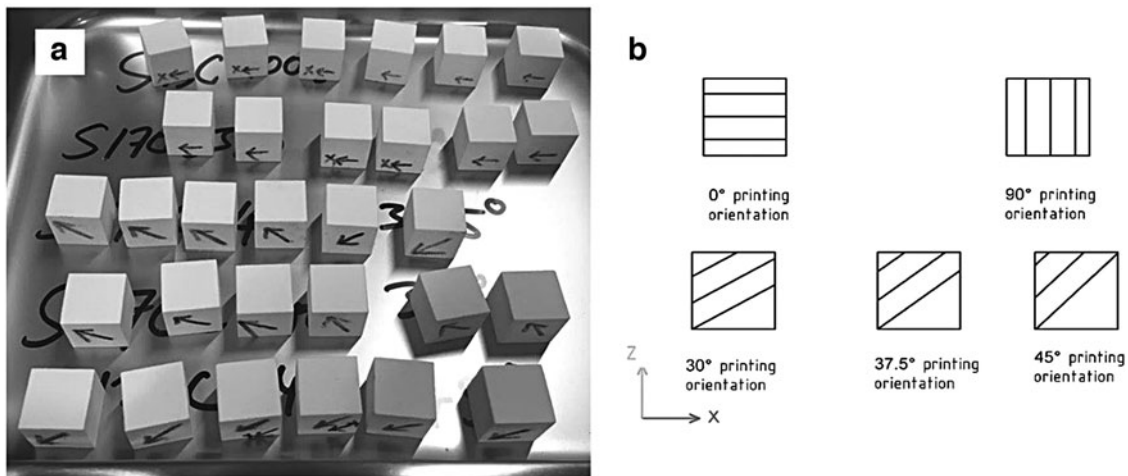
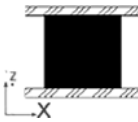
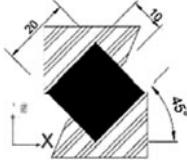
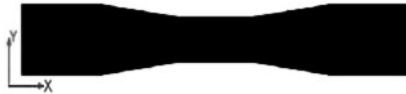



FIG. 3. (a) Real-world 3DP cubes in 0°, 30°, 37.7°, 45°, and 90° orientation, (b) CAD file of the 3DP cubes in 0°, 30°, 37.7°, 45°, and 90°.

TABLE 4. TESTS WITH RESPECT TO THE NUMBER OF SPECIMENS, DIMENSIONS, AND BUILD ORIENTATIONS (GROUP 2)

| Test | No. of specimens | Dimensions (mm) | CAD drawing |
|--------------------------|------------------|-----------------|---|
| Compression test | 30 | 20×20×20 |  |
| Shear test | 30 | 20×20×20 |  |
| Direct tensile test | 36 | 205×30×6.5 |  |
| Three-point bending test | 36 | 167×17×7 |  |

Experimental for specimens in group 2

To determine the mechanical properties of the 3DP specimens, all the specimens were designed using SolidWorks software and then exported as an STL file. Figure 6 shows the dog-bone specimens in different orientation angles, which were printed at 0°, 30°, 37.5°, 45°, and 90° rotated to the XZ-plane. It also shows in the 3D Systems software the orientation angle of the prepared specimens with regard to the X, Y, and Z planes. All the specimens for compressive, and flexural strength tests have been prepared using a similar process. In addition, all the tests have been performed and rotated in only one plane: the XZ-plane. To visualize all planes of the printed specimen, refer to Figure 1.

The orientation angles in 3DP can be used in powder-based 3DP to create different geometries, to optimize the mechanical strength of structural parts, and to optimize the number of layers required to print an object.

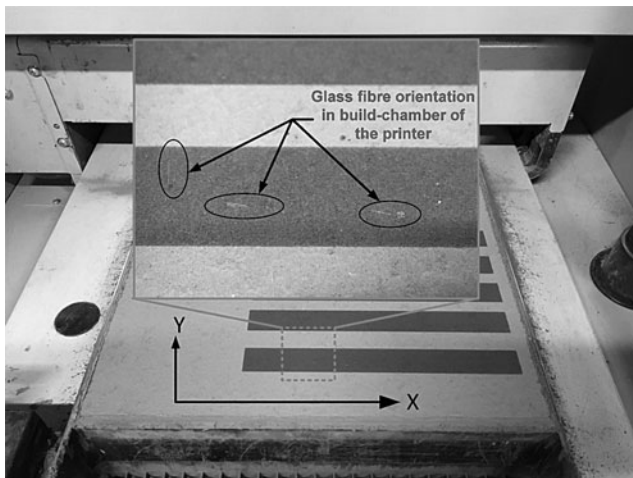


FIG. 4. Glass fiber orientation while bedding the powder on the build chamber of the 3DP.

Deflection of 3DP parts. The most vital features that distinguish the powder-based 3DP specimens from the conventional casting method are the accuracy and dimensional precision of 3DP specimens. The dimensions of the specimens have been measured by digital calipers with an accuracy of 0.01 mm. The height has been measured using both a MeasumaX and a Mitutoyo (LH-600E), which have accuracies of ±0.04 and ±0.00122 mm, respectively.

Compression test. One of the common factors that can be used to assess the mechanical suitability of concrete and

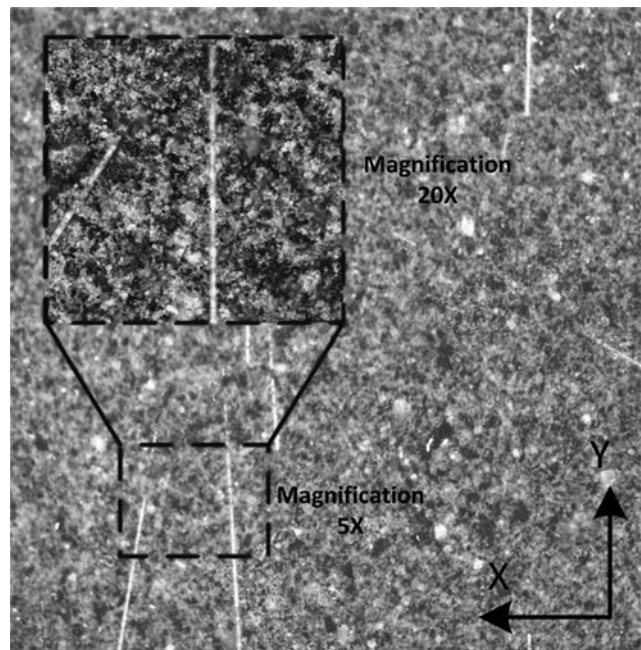


FIG. 5. Glass fiber bedding on the dry powder in the build chamber of the 3DP (3D laser scanning image LEXT OLS5000).

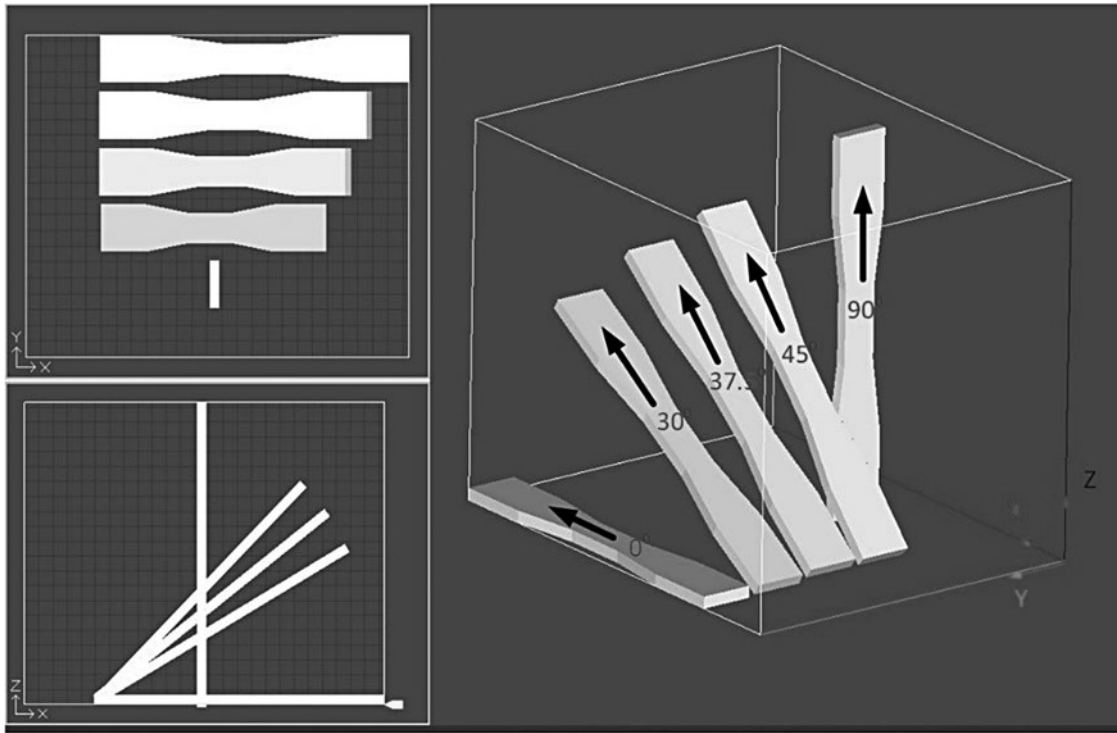


FIG. 6. Schematic drawing of the printed dog-bone specimens in different orientation angles rotated to the XZ-plane.

mortar for construction applications is its compressive strength.⁴⁰ Thus, compressive strength tests have been conducted for the 3DP specimens in accordance with the ASTM standard.⁴⁰ A total of 30 specimens have been tested, including 3 specimens for each of the orientation angles. The rate of loading in the tests was 0.833 kN/s. A Shimadzu load cell (AGS-X 50 kN, Japan) testing machine was used to perform the mechanical tests at room temperature ($22^{\circ}\text{C} \pm 2^{\circ}\text{C}$) with a humidity level in the range of $(60 \pm 10) \%$.

Shear test. The specimens were placed between the two loading plates for the purpose of testing shear resistance. The upper and lower boundaries were unrestrained in the horizontal direction, similar to a study conducted by Cao RH *et al.*⁴² The

displacement loading rate was fixed at 0.2 mm/min. Figure 7 shows how the specimens were positioned between two inclined die blocks at a 45° inclined angle relative to the horizontal direction. All specimens were loaded until the specimen reached the failure point, and the load-displacement diagram was recorded with the data collection equipment.

Overall, 30 specimens were shear tested and for each of the orientation angles, 3 specimens have been prepared and tested.

The shear stress, (τ), along the surface of the specimens can be found by Equation (1):

$$\tau = \frac{Q}{S} = \frac{P}{S} (\sin\beta - f\cos\beta) \tag{1}$$

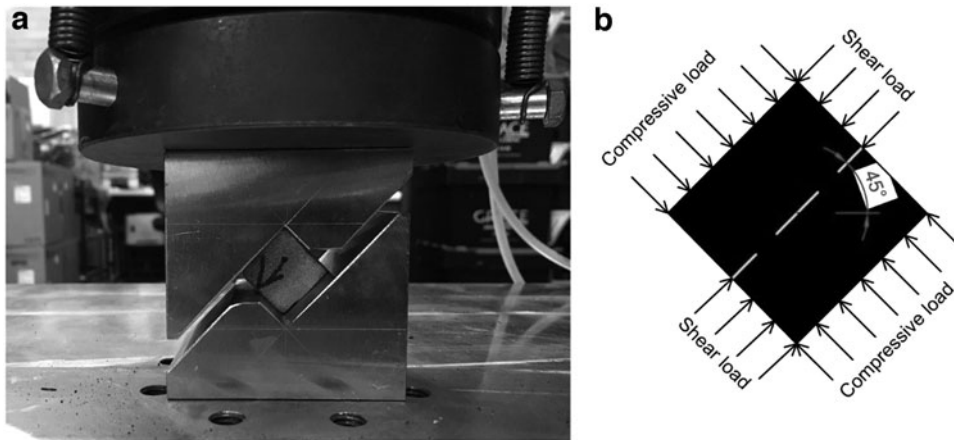


FIG. 7. (a) Loading layout in the X-axis (0° orientation) on the CP specimen; (b) experimental principle for setting and applying the load tests to specimens.

where Q is the normal shear force and S is the shear area that is equal to the cross-sectional area of the specimen. Furthermore, P is the axial force on the specimen and f is the friction coefficient between the shear case and the shear load platform. In this investigation, the friction coefficient, f , is zero because the shear box setup is connected directly to the load platform. Finally, β is the shear angle, which is equal to 45° .

Direct tensile test. The specimens for the tensile strength were prepared according to the ASTM: D638 type III.⁴³ Overall, 36 specimens underwent tensile testing for all the orientation angles from 0° to 90° . For each of the orientation angles, three specimens have been prepared and tested. The tensile test is used to determine the elongation of the specimens at the breaking point for each of the ZP 151 and CP specimens.

Three-point bending test. Three-point bending tests can be used to measure flexural strength by deliberately inducing stress in an object by bending it. The flexural strength was measured for each specimen according to the ASTM standard.⁴¹ A total of 36 specimens have been printed for this test using the manual mix, including 3 specimens prepared for each orientation angle. The rate of loading in the test was 426 N/min. The three-point bending test is used to provide a flexural stress-strain response of the ZP 151 and CP specimens.

Results and Discussion

Results for specimens in group 1

Mechanical strength result. The strength and stiffness characteristics of a material are significant in determining the

behavior of the resulting structural component. Figure 8 shows the compressive strength test outcomes for the set of printed specimens (from Table 2) that were cured for 28 days at five different temperatures. The bars with values indicated on top were the actual strengths, while the error bars indicate the standard deviations of the results. Figure 8 shows that an increase in the curing temperature from 40°C to 80°C led to an increase in compressive strength. This strength increase was almost proportional to the temperature rise within this range. However, once the temperature of curing is further increased up to 100°C , the compressive strength starts to decrease.

The increased strength in the cement mortar that is proportional to the increase in curing temperatures was most likely due to the increasing reaction level of the cement mortar within this temperature range. Curing in an oven accelerates the reaction of the cementitious process. Fast hydration and a high early compressive strength were observed as the temperature increases.⁴⁴

The experimental results were consistent with a study by Abd elaty,⁴⁵ which demonstrated that the compressive strength of Portland cement concrete with a low w/c ratio at 50°C was higher than at lower temperatures (10°C and 23°C). Compressive strength improvements and the trend of increasing strength have been repeatedly observed, even at 91 days for cement mortar at temperatures of 60°C .⁴⁶

Increasing temperature might increase the rate of reaction in the mortar mixes and consequently a reduction in the setting time. The reason is that higher temperatures accelerate the dissolving of alumina (Al_2O_3) and silica (SiO_2) particles from the unreacted particles of the powder and a greater amount of Al_2O_3 and SiO_2 becomes available for the reaction process. The modified powder for 3DP contains a high

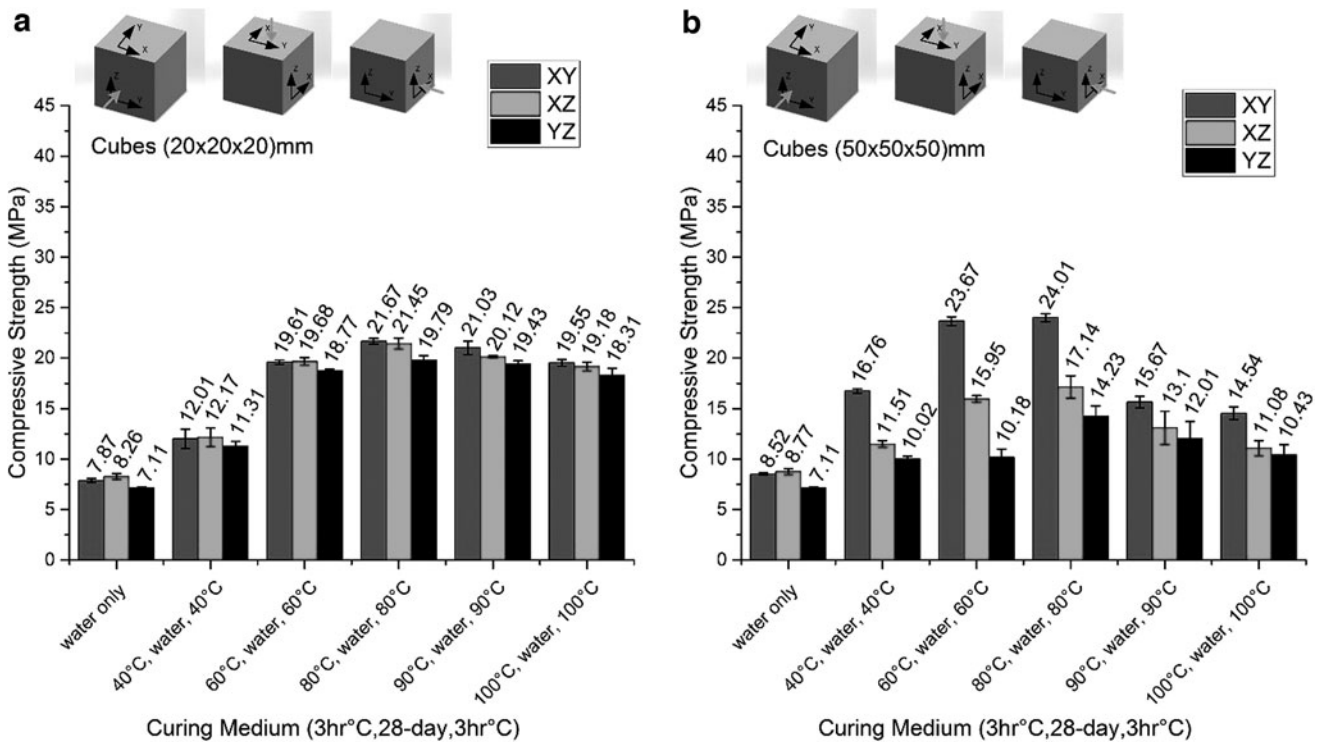


FIG. 8. Compressive strength of mortar specimens using different curing media without glass fiber for (a) $(20 \times 20 \times 20)$ mm cubes and (b) $(50 \times 50 \times 50)$ mm.

proportion of alumina due to the high levels of CAC in the main powder. In relation to the total mass, Al_2O_3 comprises $\sim 70\%$ in CAC, whereas it is only 5% in cement.

Despite the trend observed up to 80°C , a decreasing trend was observed when temperature increased beyond 80°C up to 100°C (Fig. 8). An earlier study by Altan and Erdoğan⁴⁷ found that a threshold temperature for the cementitious reaction process occurs when temperature-controlled kinetics is inhibited. Extra Al_2O_3 and SiO_2 particles react when the curing temperature is above the threshold point. Mortar slurry forms rapidly and is deposited on the surface of the unreacted powder, constraining the alumina and silica that can dissolve. Consequently, the compressive strength declines significantly. Hence, 80°C was nominated as the optimum curing temperature for cement mortar specimens.

In general, curing in tap water achieves low compressive strength test results, predominantly due to the slight reaction that occurs among particles. The small concentration of OH^- ions in tap water works as a reactive chemical agent in the cementitious process since it leads to ineffective dissolving and formation of hydroxyl substances.^{48,49} Consequently, low compressive strength will emerge due to the densifying reaction not being appropriately established. It must also be noted that water curing at high temperatures has been observed to adversely affect compressive strength due to heat acceleration, which leads to the leaching of Al_2O_3 and SiO_2 from the existing gel in the specimens.

Figure 9 shows that the printed specimens cured at 90°C and 100°C have surface cracks due to the exposure to high temperatures and the evaporation of contained water. Abdulkareem *et al.*⁵⁰ found that mortar and geopolymer paste exhibit reduced strength as the temperature is incrementally increased beyond a certain threshold temperature, and that the best result occurs at

70°C . These observations are consistent with the results of this study for the cement mortar-based 3DP objects that were tested at various temperatures, although the threshold temperature was slightly different (80°C here vs. 70°C in theirs). In addition, Figure 9 shows that elevating the temperature to 100°C led to cracks appearing in the specimen. Given that the boiling point of water is 100°C , the increase in temperature led to rapid evaporation of liquid in the specimen (the binder liquids contain over 90% water). Therefore, cracks were visible on the surface of the specimen.

Specimens for the compressive test were printed and tested in all three planes. It has been determined that the compressive strength is predictably influenced by the printed plane direction of the specimen. For the 20 mm cubes, the prints along the YZ plane exhibited noticeably lower compressive strength compared to the prints along the XY and XZ planes, which both yielded similar results (Fig. 8a).³³ For the 50 mm cubes, however, the XY plane displayed significantly better results compared to the other planes (Fig. 8b). The XY plane is parallel to the printhead.

The results displayed in Figure 8 demonstrate that the size influence of the printed specimens was contrary to the situation for conventionally cast mortar specimens.¹² The size of the printed specimens was directly proportional to its compressive strength, where an increase in size resulted in an increase in compressive strength. This phenomenon could be due to better flowability from the feeder bin and better compaction on the build chamber for the larger specimens. The feeder bin contains a rotary motor, which is located in the middle of the printer. Therefore, the powders for the larger specimens deposit from the end of the feeder bin with more homogeneity and fewer voids between particles. This results in a better deposition of powder and more powder flowing from the feeder. Powders



FIG. 9. Prism mortar specimen (160×40×40) mm after being removed from the oven at 90°C .

that contain more particles in the feeder chamber allow the roller to spread in a higher quantity, and thus results in a more effectively compacted build chamber.

Size of the 3D printed specimens is also related to the powder flowing from the feeder bucket of the 3D printer. However, this amount of powder in the feeder bucket directly affects the result of the printed specimens. This can be expressed as a vertical pressure in the silo, expressed as Equation (2).⁵¹

$$q = \rho gz \tag{2}$$

where q represents the vertical pressure in the silo, and ρ is the bulk density of the materials. The gravitational acceleration is g , which is considered constant, and z is the height of the materials in the feeder, which flow to the build chamber. Therefore, the pressure of the materials is directly related to the amount and height in the bucket flowing into the build chamber. The increasing amount of material in the bucket relatively increases the pressure of the materials to release particles from the bucket.

However, according to the Beverloo *et al.*,⁵² the mass flow rate, Q , in the rectangular silo with a single opening of size of D_0 in the silo, and a particle diameter of d , can be expressed in Equation (3) as follows:

$$Q = C\rho\sqrt{g}(D_0 - kd)^{3/2} \tag{3}$$

where g is gravity, C and k are constants, and ρ is the density. This equation is relevant to a rectangular-shaped silo, which,

considering the diameter of particles and opening size, is the same shape as the bucket of the 3D printer. This formula could be beneficial to calculate the mass flow of materials in various sizes of 3D printer.

Table 5 shows the list of previous studies that have been conducted on the size effect of concrete and mortar.

Figure 10 shows the comparisons of the earlier research on the size effect of concrete and mortar. It is important to note that these comparisons are with reference to a 100 mm cube size.

It was expected that the 3DP part that is built using the current 3D printer would achieve the optimum strength for the 100 mm cube size, due to the amount of powder in the feeder bucket. However, the amount of powder remaining in the feed bucket reduces to less than half after printing the 100 mm size part in the build chamber. Hence, the vertical pressure reduces relatively as well. The depth of the build size of the 3D printer is 254 mm; therefore, half of the powder materials would still remain in the feeder bucket after producing a 100 mm size part.

These results are positive for the construction industry and precast construction applications. This study used optimal saturation levels that have been detailed in the earlier studies^{35,61} to show the strongest plane and direction. In addition, the studies showed the optimized heating temperature during medium curing, which can attain the highest compressive strength.

Figure 11 presents the compression strength of the printed mortar using 1% E6-glass fiber as reinforcement and curing at different temperatures. Figure 11 shows that curing at 80°C recorded the optimum compressive strength for the printed mortar. It was also found that the maximum strength was in the XY plane when the load was applied to the YZ plane. The compressive strength of mortar with 1% glass fiber was recorded as 37.88 MPa, which is strong enough to be suitable for the construction industry and precast construction applications.

In this study, the optimum saturation level has been derived from the authors' earlier studies.^{35,61} Therefore, the achievements of this study are in finding the strongest plane and the optimized heating temperature, which can be used as the most suitable curing medium to achieve the highest compressive strength. For long-term durability and checking the quality of the materials, it is necessary to conduct further investigations, such as monitoring the surface quality of the printed structure in harsh environments and checking the serviceability of the printed structural members in real applications.

The compressive strength results using 1% glass fiber significantly increased strength values by ~37%. Flexural strength was increased by 46% at 60°C with a fiber content of 1%. This represents an increase in both compressive and flexural strength.

All specimens, either with or without glass fiber, have been subjected to the same curing conditions. After the curing, the fiber-reinforced printed specimens showed significantly higher mechanical strength values than the unreinforced specimens. In addition, a fiber content of 1% was easily mixed in the feeder tank and passed through the feeder holes. A higher ratio of fiber content in the cement mortar might not easily flow through the feeder tank. Furthermore, a higher content of fiber filaments would make it more difficult to vacuum all materials back to the feeder tank.

TABLE 5. THE REFERENCES AND THE LABELS FOR EACH OF THE SPECIMENS

| Labels | References |
|------------------------|---------------|
| A1(198.1) | 53 |
| A2(153.8) | |
| A3(84.2) | |
| B1(91.8) | 54 |
| B2(119.6) | |
| B3(137.1) | |
| C1(61.2) | 55 |
| C2(50.0) | |
| C3(44.2) | |
| D1(96.1) | 56 |
| E1(32.2) | |
| E2(49.5) | 57 |
| E3(73.1) | |
| F1(47.0) | |
| F2(62.5) | |
| F3(66.5) | |
| G1(43.0) | 59 |
| G2(49.0) | |
| H1(116.3) | 60 |
| H2(123.8) | |
| H3(144.2) | |
| I(47.16)M ^a | 12 |
| J1(3DP)M | Present study |

^aM represents mortar, while the rest are concrete materials. 3DP, three-dimensional printing.

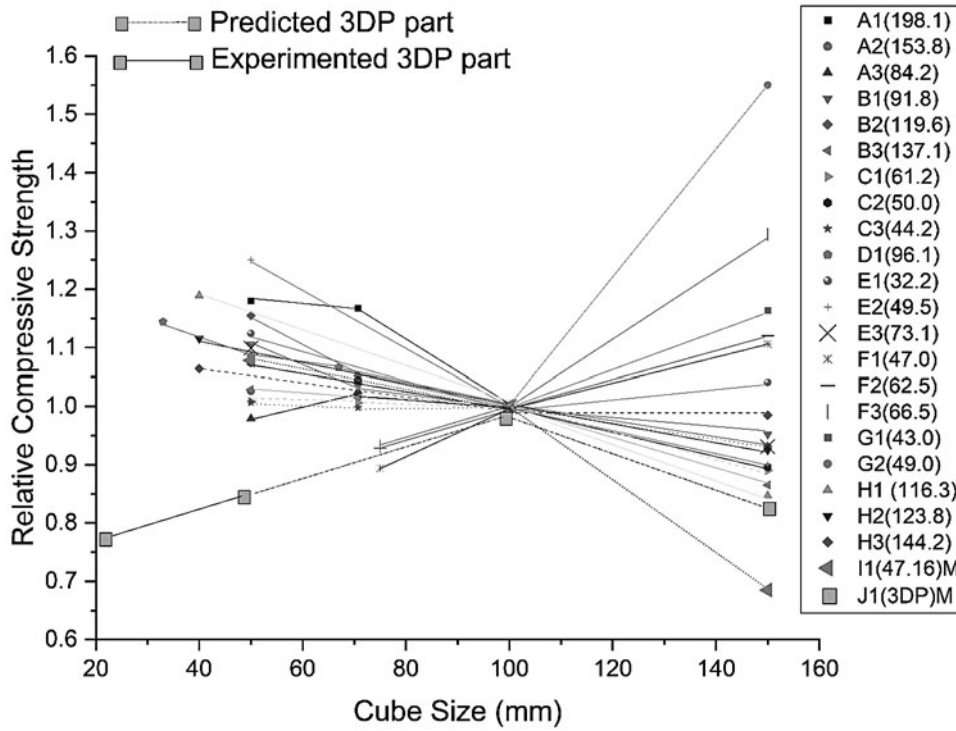


FIG. 10. Relative compressive strength of concrete⁶⁰ and mortar specimen different sizes.

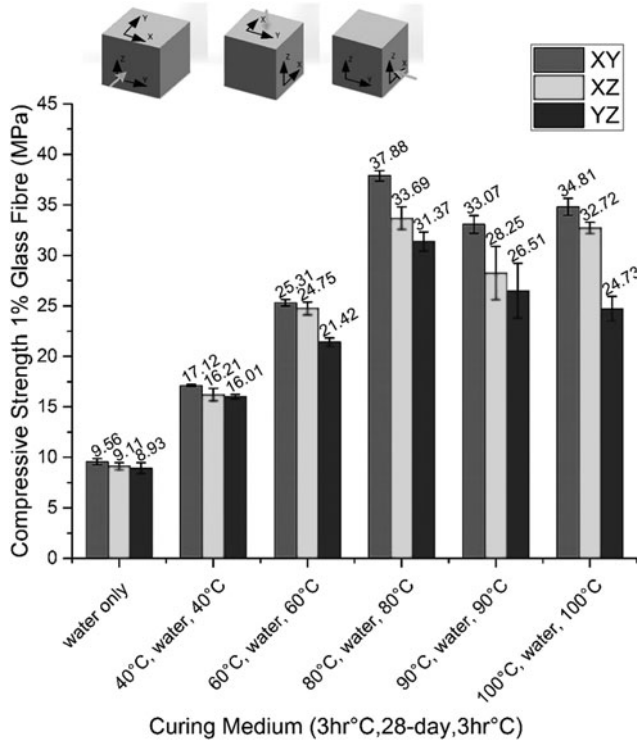


FIG. 11. The compressive strength of the mortar specimens (50×50×50) mm with 1% glass fiber and using different curing media.

Figure 12 shows the flexural strength of the specimens tested. An examination of the mechanical properties using the three-point bending test revealed higher flexural strengths at 80°C. The curing temperature at 80°C achieves better results among all the curing temperatures considered.

Investigation of mechanical properties using the three-point bending test found higher flexural strengths in fiber reinforced specimens (Fig. 12). This represents a transfer of the mechanical load from the matrix into the fiber, in addition to energy dissipation caused by frictional forces when the fiber stretches,²⁴ resulting in greater strain in the composite. The researchers found that the orientation of fiber reinforced filaments in specimens can have an effect on mechanical properties.⁶² However, there was a slight difference between the orientations of printing direction when specimens were fiber reinforced. The fiber filaments were oriented mostly in the Y-direction; thus, the reinforcement along the Y-axis is better (primarily stronger) when compared with the specimens printed in the X-direction (Fig. 8). This is consistent with the study performed by Feng P *et al.*²⁶ for calcium hemihydrate (Note: in that study, the X and Y axes were oriented in reverse). Drying in the oven after printing greatly improved the mechanical properties, but may have affected the effectiveness of fiber reinforcement in the specimen, particularly at very high temperatures (over 80°C). This suggests that postprocessing (at heat temperature) and hardening have a greater impact on mechanical properties than fiber filament reinforcement.

Surface roughness. Ra is a value that describes the surface roughness of the material surface examined. A substantial change occurred when glass fiber was added to the

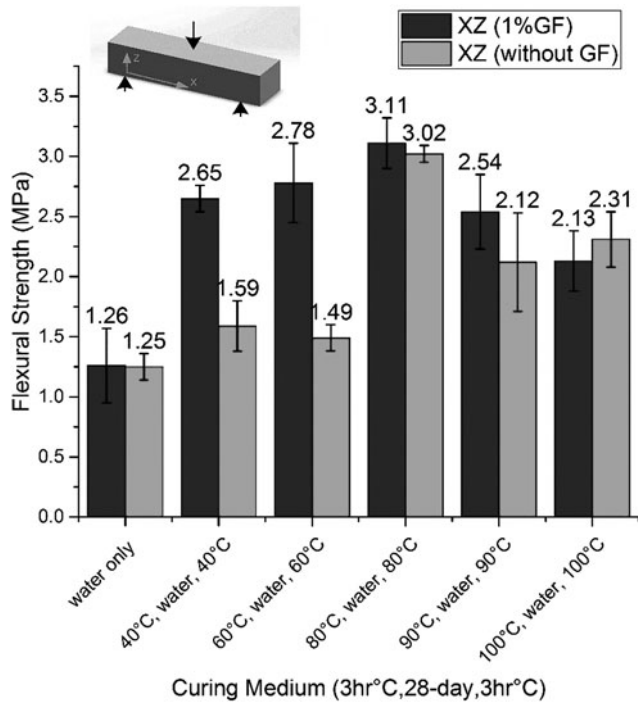


FIG. 12. Flexural strength of mortar specimen (160×40×40) mm with and without glass fiber for different temperatures and media.

cement mortar. Figure 13 shows the 3D laser microscope and scanning electron microscope (SEM) images of the surface morphology of printed CP specimens at the magnification level of 20× and 25×, respectively. Noticeable holes and valleys are visible on the CP printed specimens. The blurring in the images occurs where there are different heights on the surface.

Figure 14 shows the roughness profile of the printed CP and ZP 151 specimens (Table 2). The average surface roughness on the surface of the CP was $22.31 \pm 3.72 \mu\text{m}$,

which is slightly higher than the ZP 151 result, namely, $13.76 \pm 0.95 \mu\text{m}$. This means that the cement powder’s surface was rougher than gypsum and has more valleys on the surface of printed objects.

The 3D surface image of the powder on the build chamber can be captured and analyzed using a 3D scanner microscope. After printing a complete layer on the build chamber, the build chamber was taken out of the 3D printer. It was then placed under the 3D laser scanner microscope to analyze the powder roughness and profile roughness of the powder.

The roughness on the surface mortar varies from position to position due to the inconsistency of distributing cement mortar powders on the build chamber. The powder particle distribution of the recommended material (gypsum) on the build chamber was even, with the printed specimen having a higher resolution and smoother surface (Fig. 14).

Figure 15 shows the 3D surface profiles of the powder bed for the recommended ZP 151 and CP powders. The figure shows a 3D profile difference of $\sim 161 \mu\text{m}$ between CP and ZP 151 peaks and valleys. A noteworthy difference between CP and ZP 151 powders was discovered by using a 3D scanning process. ZP 151 has a more even surface than the CP powders due to better uniformity of its particle size distribution of the powders than the CP. This uneven distribution leads to open pores between layers and among the particles, which affect the mechanical strength of the final product of the printed powder.

Figure 16 shows the surface roughness profiles of CP and ZP 151. The roughness of CP powders was obvious and arbitrarily distributed all over the build chamber of the 3DP. However, the ZP 151 powder has an overall uniform distribution across the build chamber of the 3DP.

Figure 17 shows the surfaces of the printed CP and ZP 151. It was clear that the powder layer bedding distribution on the build chamber is reflected in the printed specimens for CP and ZP 151. The layers in the ZP 151 specimen were infused with the following layers (Fig. 17), whereas the bond between each layer for the CP specimen can be easily distinguished.

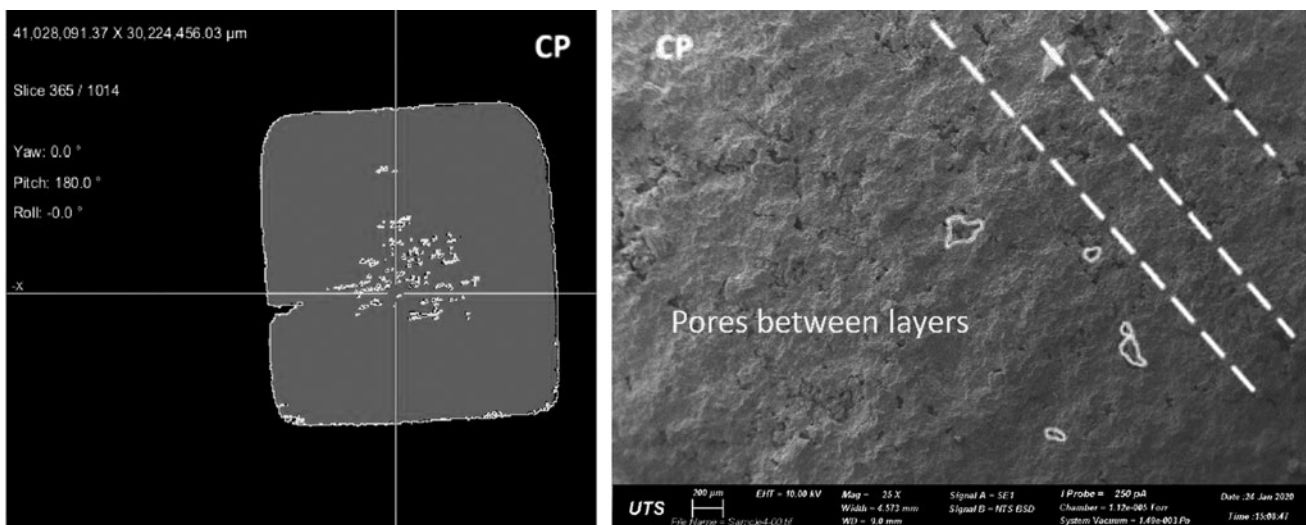


FIG. 13. μCT scan of the layer 265 (mid of specimen) and SEM of the surface of printed CP at 20× and 25×, respectively. μCT , microcomputed tomography; SEM, scanning electron microscope.

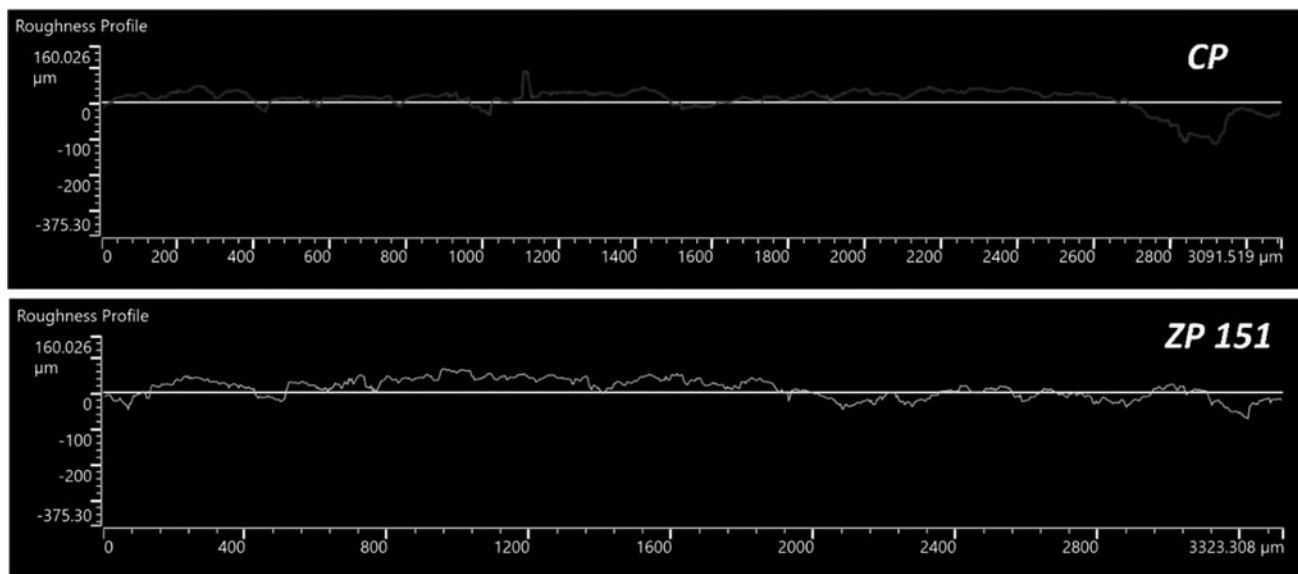


FIG. 14. Surface roughness profile of printed CP and ZP 151; images show the roughness profile compared with the mean line.

Table 5 lists the value of skewness (Ssk) for CP and ZP 151 (green part) specimens. The topology and height distributions can be observed by means of the value of skewness (Ssk). After curing, they have an asymmetric end extending toward more positive values, which means many high spikes emerged on the surface topography. The Ssk parameter has been linked to porosity and load bearing. The study by Petzing *et al.*⁶³ explained that when Ssk is zero, the height distribution at the surface is symmetrical. This was shown by the center line for both asymmetrical and symmetrical purposes. Table 6 shows

the Ssk values for the printed specimens (green part) on the surface of the specimens before postprocessing.

Figure 18 clearly shows the schematic illustration of the orientation of the fiber filaments after spreading occurs in the build chamber. Most of the glass fibers were spread parallel to the Y -axis, the reason being that the fast axis roller pushes all powder and fibers in this direction. This is consistent with the results of Christ *et al.*²⁶

3D laser scanning microscopy has been used to capture the fiber filaments in the printed object. The benefit of using the

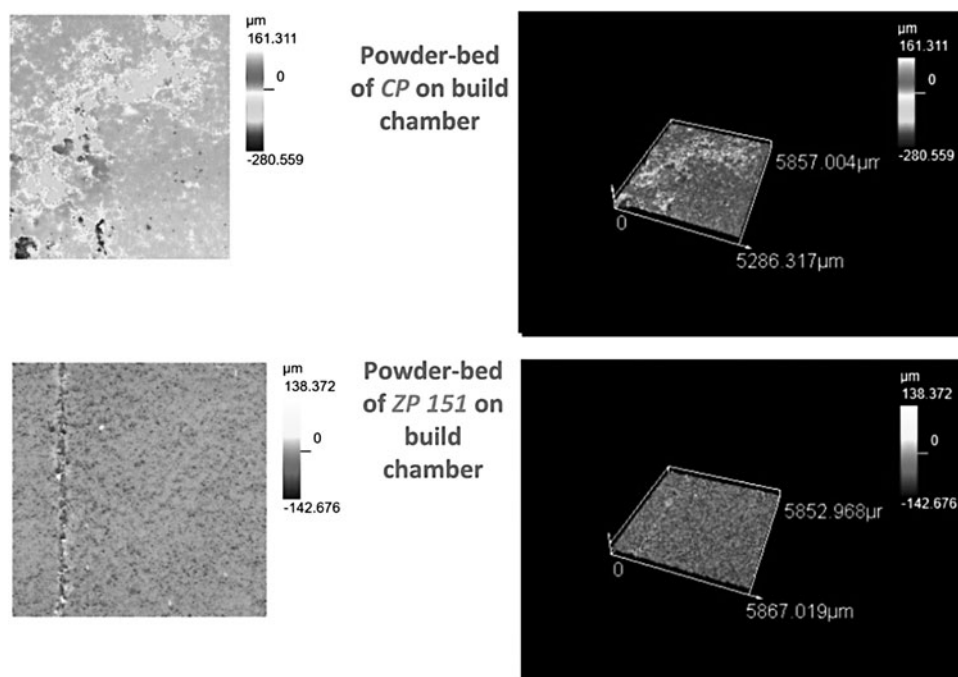


FIG. 15. Three-dimensional surface profile and images captured of the powder bed on the build chamber for CP and ZP 151 powders.

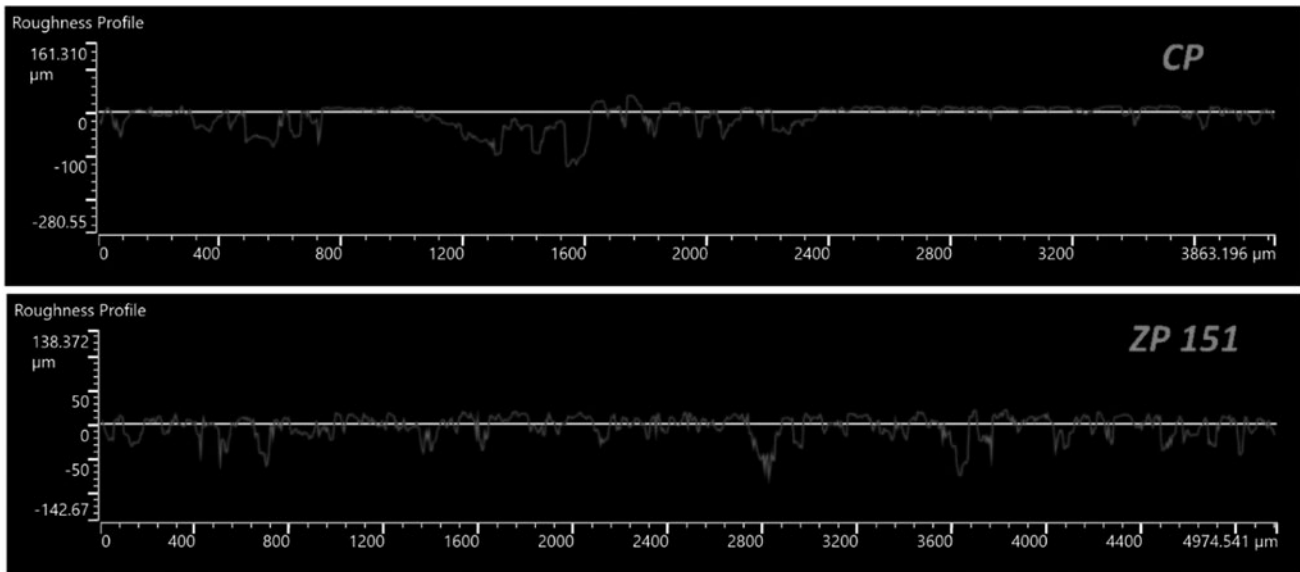


FIG. 16. Surface roughness profile for powder bed CP and ZP 151 materials.

scanner was to capture the fiber filaments extremely close to the required magnification and to detect the bedding orientation of the fiber. It was also able to detect whether the fiber was damaged (Fig. 19).

The porosity and density of the composite materials have an impact on the mechanical properties of the specimens. However, while the density of the printed scaffold was not affected by fiber reinforcement (Table 2), there was a reduction in the porosity of the printed scaffold when it was fiber reinforced due to the well-distributed fibers in the powder bed chamber. Figure 20 shows the surface roughness profile of printed specimens in the presence and absence of glass fiber. The figure shows a reduction in the roughness of surface morphology of the cubic specimen. The surface roughness of the cubic CP specimen with 1% glass fiber was $18.57 \pm 1.35 \mu\text{m}$ and that of the specimen without glass fiber was $22.31 \pm 3.72 \mu\text{m}$.

To check the diameter of the filaments and the spreadability of the chopped glass fiber in the printed specimens, the specimens were examined using 3D laser scanning microscopy (LEXT OLS5000). The results show that the diameter of the filaments was the same as that of the manufacturer of the E6-glass fiber, namely, $13 \mu\text{m} \pm 10\%$ with a length of $6000 \pm 1000 \mu\text{m}$.⁶⁵ This means the fiber filaments disperse and maintain in the printed specimens without any damage.

Figure 21 shows the 3D laser scanner image of the fiber filaments in the printed specimens. That figure clearly shows the approximate length at the edge of the specimen and the diameter of the specimen. The length of the filaments extending beyond the edge was $\sim 400 \mu\text{m}$, with the rest of fiber's length inside the printed mortar. The diameter was $\sim 13.49 \mu\text{m}$. This is proof that the filament was not damaged during printing and solidifying.

The study by Zortuk *et al.*⁶⁶ used different percentages of glass fiber (0%, 0.5%, 1%, and 2%) in the thermoplastic resin, and then examined the physical characteristics and the surface roughness. They found that the mechanical strength increased with 0.5% and 1% glass fiber and that there was a significant change in surface roughness and quality. This is

consistent with the findings of this article in terms of the mechanical characterization of the printed part for 3DP cement mortar. In another study by Farina *et al.*,¹⁸ two different textures of the fiber rebar were printed using electron beam melting. The macroscopic result showed that the smaller fiber rebar had better pullout response after fracture, which confirmed the presence of fiber among mortar particles connecting cracked valleys. The SEM image also showed that the morphology of large fibers can be affected by a weaker fiber matrix.

Figure 22 shows the relationship between surface roughness and compressive strength. It shows that the printed specimens with lower surface roughness values have higher compressive strength than specimens with higher surface roughness values. This is consistent with earlier studies that characterized materials based upon their surface roughness and found that materials with a higher surface roughness have lower fatigue stress.⁶⁷ This result is opposite to the bond strength in shear and pullout tests of concrete where a higher surface roughness has been shown to enhance the bond and pullout strength.⁶⁸

The compacting stress and surface roughness tests have been conducted on the NiTi alloy.⁶⁹ It was discovered that by increasing the surface roughness, there is a reduction in compacting stress. It is theorized that this is due to a reduction of pores in such circumstances.

Figure 22 shows that the compressive strength is affected by the surface roughness of the specimen. The low surface roughness has a high compressive strength, while the high surface roughness has reduced compressive strength.

Binder dosage and resolution. The binder has a significant effect on the mechanical strength results when curing occurs at high temperatures due to the content of the binder, namely, water and humectant. The binder in this study consisted of humectant (2-pyrrolidone³⁸) and water. In the study by Bredt *et al.*,⁷⁰ the binder was not pure water, as it included 5–10% of polyvinyl alcohol or glycerol (humectant) or methanol (20% volume of binder).

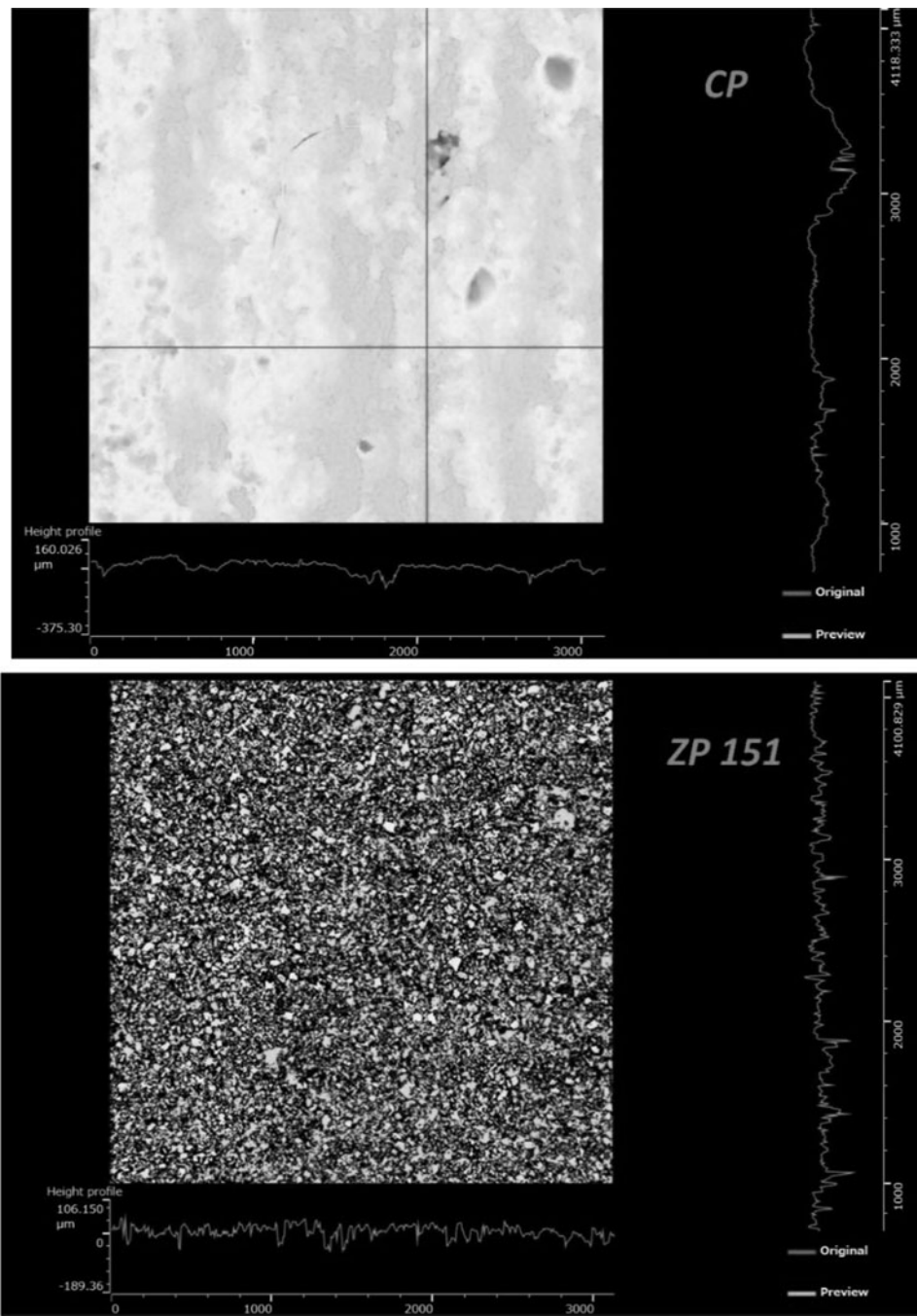


FIG. 17. Surface roughness profile for the printed specimens of CP and ZP 151.

TABLE 6. SKEWNESS VALUE AND SURFACE ROUGHNESS VALUE LISTED FOR CP AND ZP 151 FOR GREEN PART SPECIMENS

| Specimen description | Ssk | Ra (μm) |
|----------------------|-------|----------------------|
| CP | -0.56 | 22.31 ± 3.72 |
| ZP 151 | -0.18 | 13.76 ± 0.95 |

The resolution of the ProJet 360, which was used in this study, is 300×450 DPI. The resolution of the printed objects depends mainly on the binder compositions and the width of the binder on the printed parts. According to the study by Jooho *et al.*,¹⁰ the binder dose per square centimeter can be calculated using the following Equation (4):

$$\text{Binder dose (cm}^2\text{)} = \frac{\text{flow rate } \frac{\text{cm}^3}{\text{s}}}{\text{print speed } \frac{\text{cm}}{\text{s}}} \quad (4)$$

To control the size and shape of the binder droplet and jetting liquid, it is crucial to know the properties of the binder,

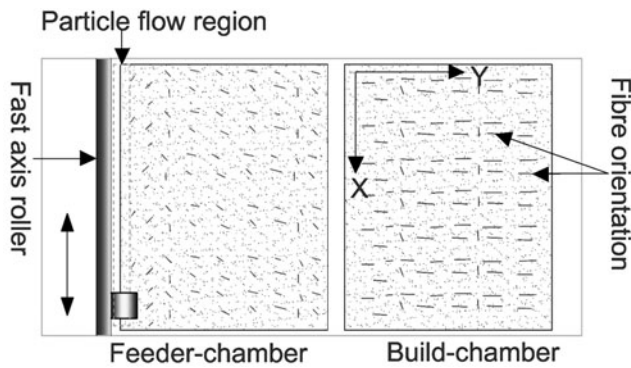


FIG. 18. Schematic illustration of chopped fibers spread on the build chamber and feeder chamber.

especially the rheology and surface tension. When the binder liquid has a low surface tension, it is easy to pass it through the printhead of the printer system. Therefore, finding an alternative humectant to glycerol and polyvinyl alcohol would be effective, as it would lead to the improved reaction among particles of the cementitious mortar.

The binder dosages affect the quality, material characterization, and bond between layers. These dosages are similar to how the ink behaves on paper in two-dimensional inkjet; therefore, it is important to know the spreading and penetration of the droplet on the surface (Fig. 23).

The binder drop test results for both types of powder (CP and ZP 151 for specimens in Table 2) are shown in Figure 23. It shows that the drop diameter on the CP powder was greater than on the ZP 151. Therefore, the penetration in CP is quicker than in ZP 151 (see Fig. 22 for the depth and diameter of the droplet on the powder). The diameter of droplets on CP and ZP 151 recorded 2.64 ± 0.02 mm and 2.40 ± 0.09 mm, respectively. The average depth of the droplets on CP and ZP 151 has been recorded as 1.11 ± 0.21 mm and 1.25 ± 0.03 mm, respectively.

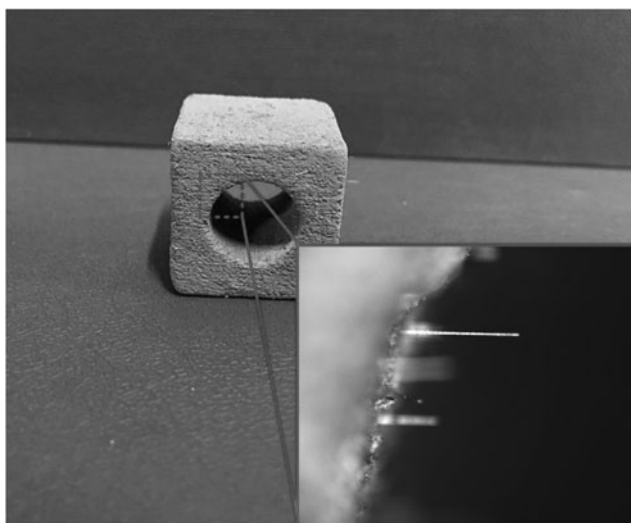


FIG. 19. Fiber bedded orientation using 3D laser scanning (LEXT OLS5000).

Deflection, compression, shear, and tensile testing (results for specimens group 2)

Deflection of 3DP parts. All the specimens in Table 4 that underwent tensile and three-point bending tests have been measured to determine the amount of deflection. This deflection is then recorded for each of the ZP 151 and CP specimens, and for each printed orientation. It has been observed that the deflection was most pronounced when the specimens are large, elongated, and thin. The deflection was found to be more dramatic in specimens printed in certain orientations, particularly in the XZ-plane, except for the angles of 0° and 90° , where the deflection was insignificant.

The measurements were taken for the 3 specimens for each of the different printed orientation angles. It has been observed that specimens printed at an angle of 45° have the highest deflection for both types of printed powders. Figure 24 shows how the ZP 151 specimen's average deflection for the 45° angle was determined to be 1.77 ± 0.21 mm. However, the deflection for CP's specimens was found to have the highest value (1.79 ± 0.11 mm) for a 45° orientation angle.

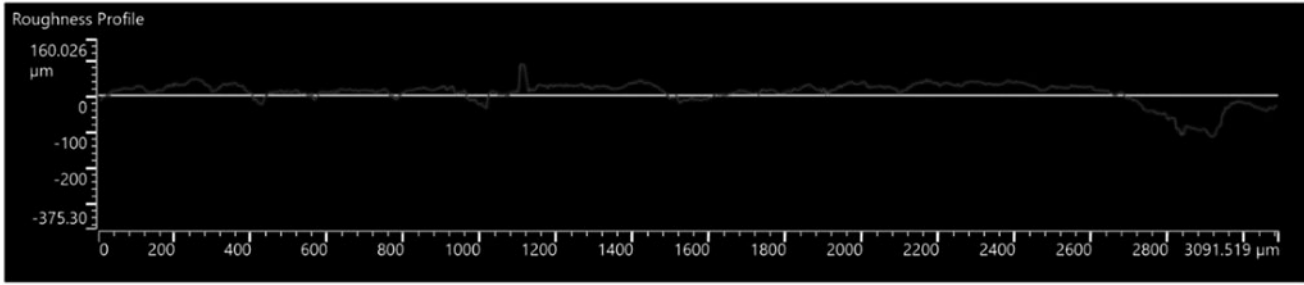
Table 7 details the mean and standard deviation of the deflections in millimeters (mm) for each of the 3DP tensile specimens. Specimens printed with an orientation angle of 0° and 90° have been found to exhibit the smallest deflections in the CP specimens, with values of 0.03 ± 0.31 mm and 0.04 ± 0.12 mm, respectively. It is noted that deflection also occurs during the preparation of the conventionally prepared specimens, but within a limited and insignificant range (<0.02 mm).

Compression test. In the previous study conducted by Shakor *et al.*,⁶¹ the porosity and voids in the cubic specimens were investigated. The optimum saturation levels found in that research have been used to print and prepare all the specimens for this article (as shown in Table 4).

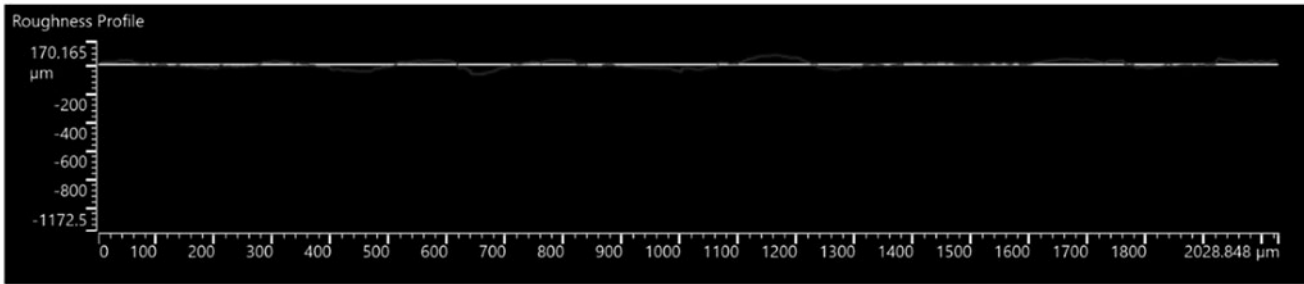
Figure 25 shows the porosity of the specimens versus the w/c ratio, where the highest saturation level (w/c) resulted in a reduction of the porosity percentage for both powders CP and ZP 151. According to the study by Popovics and Ujhelyi,⁷¹ the relationship between w/c ratio and porosity can be described by Equation (5):

$$p = 0.001a + \frac{w/c}{w/c + 1/G} \quad (5)$$

where p is the total porosity for the fresh cement, a is the air content by volume, G is the specific gravity of cement, and w/c is the water/cement ratio by mass. Consequently, an increase in w/c ratio means an increase in porosity of the specimen and results in a reduction in strength of the specimen. However, this equation cannot be applied to the 3DP cementitious powder (CP) or gypsum (ZP 151). The printing of CP and ZP 151 was completed as a layer-by-layer process. This technique is completely different from the manual mix process, which involves mixing the powder with water within one batch and vibrating it in the casting mold. The process of printing and postprocessing has various effects on the mechanical properties and durability of the printed object. For example, the hygroscopic of the powder and electrostatic charge on the surface of the powder have a major effect on the capability of powder to increase or reduce absorbing moisture



Roughness Profile of Printed Cement Mortar Cube



Roughness Profile of Printed Cement Mortar Cube with 1% glass fibre

FIG. 20. Comparison of printed cement mortar specimens in the presence and absence of glass fiber.⁶⁴

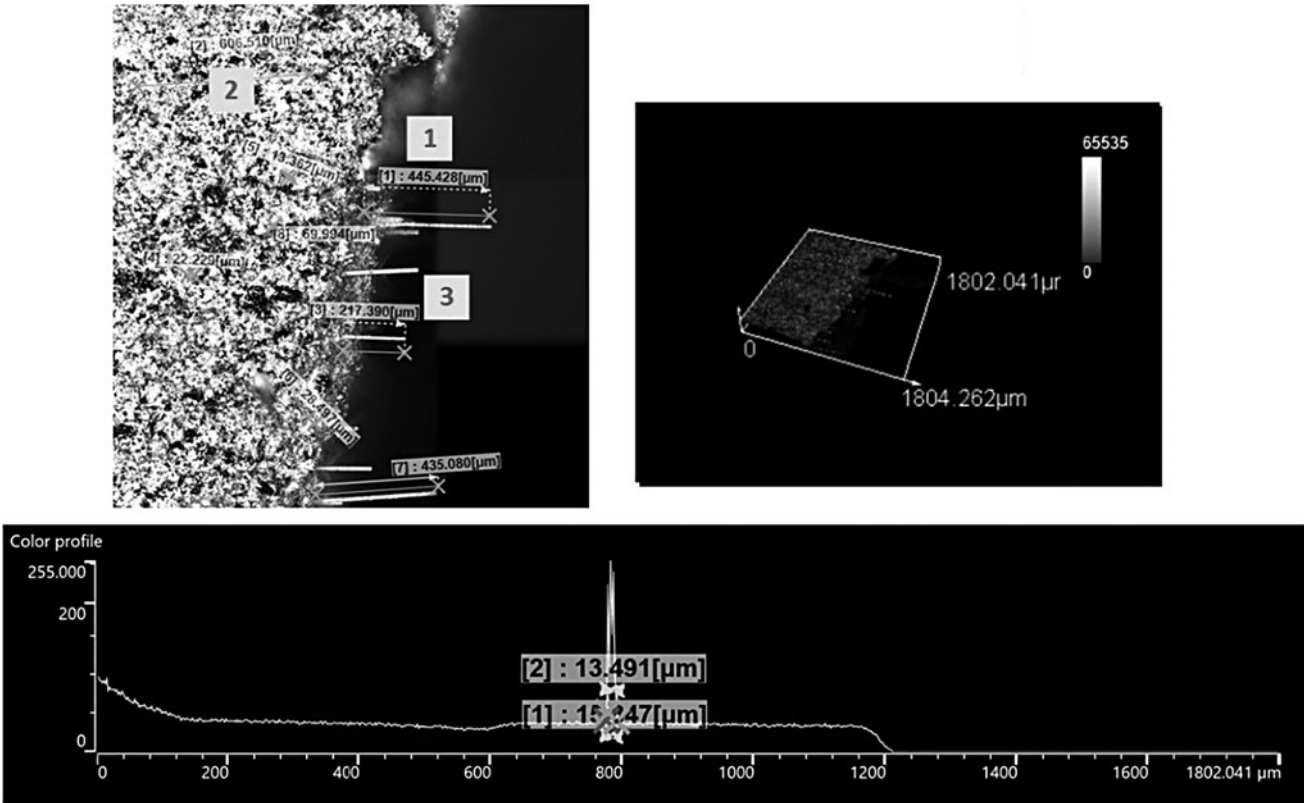


FIG. 21. Filament diameter and length of the fiber in the printed specimens.⁶⁴ In the *top left image* is numbered annotations highlighting the following: (1) fiber filament extends 445 μm beyond the edge of the specimen; (2) fiber filament length of 606 μm in the specimen; and (3) fiber filament length of 217 μm beyond the edge of the specimen.

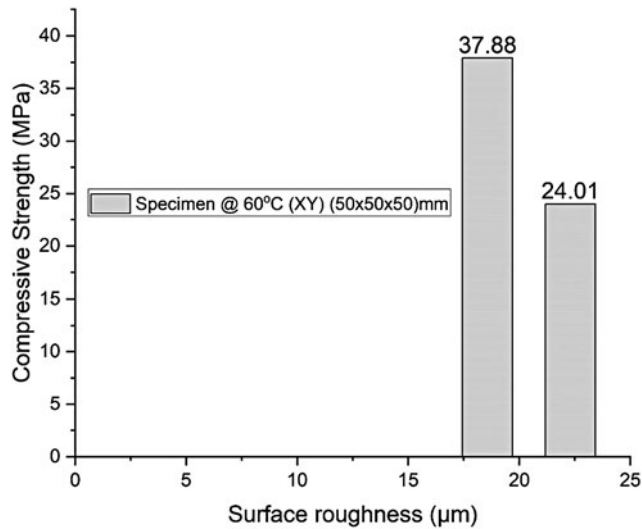


FIG. 22. Comparison between surface roughness and compressive strength.

from the air. This leads to an increase in the cohesion and a reduction in the flowability of the powder. In addition, this property in the powder would affect the size of the specimen and change the mechanical properties of the specimen. Accordingly, it is clearly shown that in Figure 25, an increase in w/c ratio in the 3DP specimens would reduce the porosity and lead to an increase in the mechanical strength of the 3DP part.

The goodness fit is displayed in Figure 25 and the regression coefficient R^2 for the CP specimen is 0.87, while the correlation coefficient R^2 for the ZP 151 is higher at 0.99. Equations (6) and (7) are the line of best-fit equations, for each powder CP and ZP 151, respectively.

$$P = -2.933 \times w/c + 57.911 \tag{6}$$

$$P = -19.445 \times w/c + 72.505 \tag{7}$$

where P represents the porosity % and w/c represents the mass of the water/cement ratio.

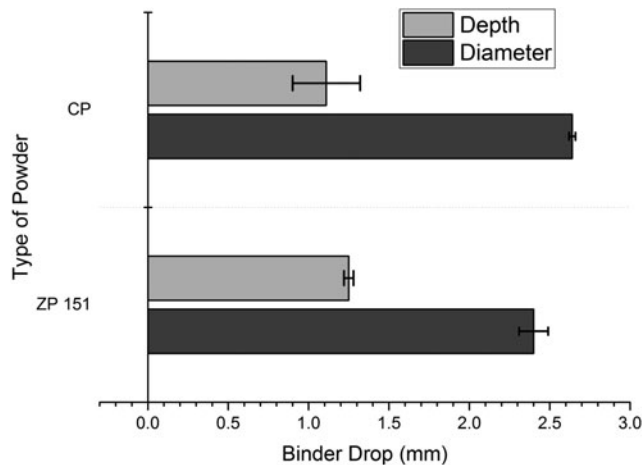


FIG. 23. Powder type (CP and ZP 151) related to the binder diameter and depth of drop penetration.

Figure 26 illustrates the compressive strength of the specimen for the saturation level of S170C340. The w/c ratios of the CP and ZP 151 materials are different because the densities of both materials are different, see Table 3. Therefore, the saturation level is equal to a w/c of 0.52 in CP and 0.46 in ZP 151 for all orientation angles. Figure 26 also shows that the orientation angle of (0°) gives the highest value (14.73 ± 0.12 MPa) for CP after curing in an oven for 3 h before and after wet curing, and 7-day curing in water. This value is enough to build a structural member, which is cured only for 7 days. According to ACI code, a 7-day cure is counted as 65% of the strength of mortar or concrete,⁷² while the compressive strength of mortar or concrete increases to about 99% strength in 28 days.

On the other hand, the ZP 151 recorded the highest result (11.59 ± 1.18 MPa) for the orientation angle (0°), that is, with the printhead parallel to the X-axis. This is similar to the results in Ref. 73, where 11.78 ± 1.19 MPa was reported for an orientation angle of 90° for ZP 151.

It is worth noting that curing for 3 h in an oven at 60°C before immersing in the water has a significant increase on the compressive strength of the specimen. This post-processing results in fewer particles dispersing in the water after insertion into the water medium as studied by the author in Ref. 39. According to the investigation by Dias,⁷⁴ the air-dried OPC concrete is found to increase in weight and reduce in sorptivity when it is kept for longer in the water medium. Another study⁷⁵ confirmed that the relative humidity has a major impact on the concrete porosity and air permeability of the specimens, which in turn has a significant effect on the mechanical strength of concrete and mortar. The study showed that drying the concrete at 50°C for 1.3–3 days would still result in 80% of relative humidity for their specific specimens. That amount of humidity would be enough to achieve minimal porosity in the specimen.

It is clear from the experimental results that the printing orientation angle has a major impact on the mechanical strength of the specimens, particularly in the cement mortar specimens. As shown in Figure 26, the printing orientation of (0°) has the highest value of compressive strength, which means the perpendicular direction has the optimum strength in the XZ-plane for cement mortar. However, the results for gypsum are slightly different since both angles (0°) can obtain maximum compressive strength. The results for the samples printed in the two angles are nearly identical, with differences in the decimal range. Thus, it is strongly recommended that the print occurs with a 0° orientation angle for CP to achieve the highest compressive strength, while also aiming to increase the flexural strength. This is further explained in the following subsection.

Figure 27 shows the result for a different set of curing conditions for the cube ($20 \times 20 \times 20$) mm at the age of 7 and 28 days. The X-axis of the figure shows the curing procedure in sequence (60°C , water, and 60°C), which means dried in an oven for 3 h at 60°C , then put in water for 7 or 28 days, and then dried again in the oven for 3 h at 60°C . Studies of the procedure (water and 40°C) have been conducted by Shakor P *et al.*,⁶¹ where specimens cured in water for 7 or 28 days and then dried in an oven for an hour at 40°C . However, the result is positive since it led to a proportional increase in the

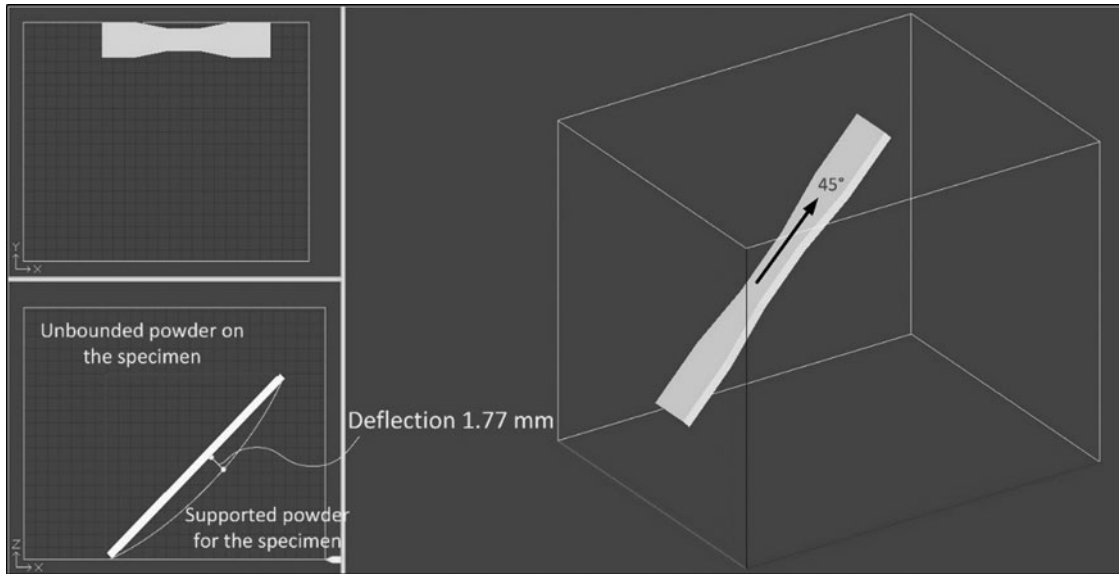


FIG. 24. Illustration of the deflection for the ZP 151 specimen (printed at 45°) in the build chamber of the 3DP.

compressive strength of specimens as the temperature of the drying process increased to 60°C. The 28-day result of the printed part shows the strength is sufficient to use in construction applications, such as in cases that currently use precast members.

Shear strength test. The shear strength test is another testing method on the specimens in Table 4 to induce a sliding failure parallel to the plane onto which forces are generally expected to be experienced. Shear forces are where one part of the material is forced in one direction and the other part is forced in the opposite direction so the material is stressed in a sliding motion. Figure 28 shows the shear strength for each specimen printed in CP and ZP 151 powders. As shown in the graph, the highest value has been recorded at 90° and 45° for the orientation angles in the CP cubes. However, the highest value was observed at 30° for the ZP 151 cubes.

It is worth noting that each powder has different characteristics in different orientation angles. Moreover, the angle of 45° provided more resistance due to the print direction being opposite to the directional load that is applied to the specimens. The value for the shear load for CP specimens at 45° was 20.28 MPa, respectively. It is obvious the angle of

45° in shear has a higher value due to the interlayer resistance in the angle 45°, which reaches rupture later than in the compressive strength test. Thus, this shear strength value can be achieved because of the changed orientation angle. For normal mortar, the cement to the sand ratio (1:6) achieved only 0.27 MPa after being coated by epoxy resin.⁷⁶ However, this is opposite to the 3DP specimens for the cement to the sand ratio of (1:0.05), where the highest strength recorded in the 45° orientation is 20.28 ± 0.54 MPa. It is noted that this result is subject to slight variations due to changes that can occur in the ratio of mixing when optimizing the flowability of the printing material in the printer.

Conversely, the maximum shear load for the ZP 151 cubes was recorded in the orientation angle at 30° and 45°, which is 9.06 ± 1.74 and 8.85 ± 1.29 MPa, respectively.

Figure 29 shows examples of the rupture between the interlayer of the printed specimens in a compression test (for ZP 151) and shear test (for CP). The fracture is quite clear in the angle section 45°, the cracks occur parallel to the printed angle 45° due to the interlayer structure in the specimen.

Direct tensile test. All the dog-bone specimens in Table 4 underwent the tensile test. The orientation angle has a major impact on the tensile result of the printed product for both materials. Figure 30 displays the results from the manual prepared specimens, 0° up to 90°. The experimental results show the maximum tensile strength for the ZP 151 is at 0°, which is 4.49 ± 0.15 MPa. The lowest result emerged in samples printed at 37.5°, while the 45° specimens of ZP 151 and CP broke before the applied load test because they were so brittle and the rate of deflection was too high; hence, specimens could not be grasped firmly, due to the curvature in the specimen, by the end of the gripper before applying the load. This was also happening to the CP specimens with an angle of 37.5°.

The CP specimens presented in Figure 30 have the highest results recorded in the manually prepared specimens, 2.35 ± 0.14 MPa, while 0° recorded the highest tensile

TABLE 7. DEFLECTION (AVERAGE ± STANDARD DEVIATION) IN MILLIMETERS FOR TENSILE SPECIMENS AT EACH DIFFERENT PRINTED ORIENTATION ANGLES

| Printed orientation angle | Deflection in tensile specimens (mm) | |
|---------------------------|--------------------------------------|--------------|
| | ZP 151 specimens | CP specimens |
| 0° (XZ) | 0.03 ± 0.23 | 0.03 ± 0.31 |
| 30° (XZ) | 0.73 ± 0.07 | 0.76 ± 0.16 |
| 37.5° (XZ) | 1.28 ± 0.09 | 1.30 ± 0.22 |
| 45° (XZ) | 1.77 ± 0.21 | 1.79 ± 0.11 |
| 90° (XZ) | 0.01 ± 0.10 | 0.04 ± 0.12 |
| Manual mix | 0.02 ± 0.11 | 0.02 ± 0.13 |

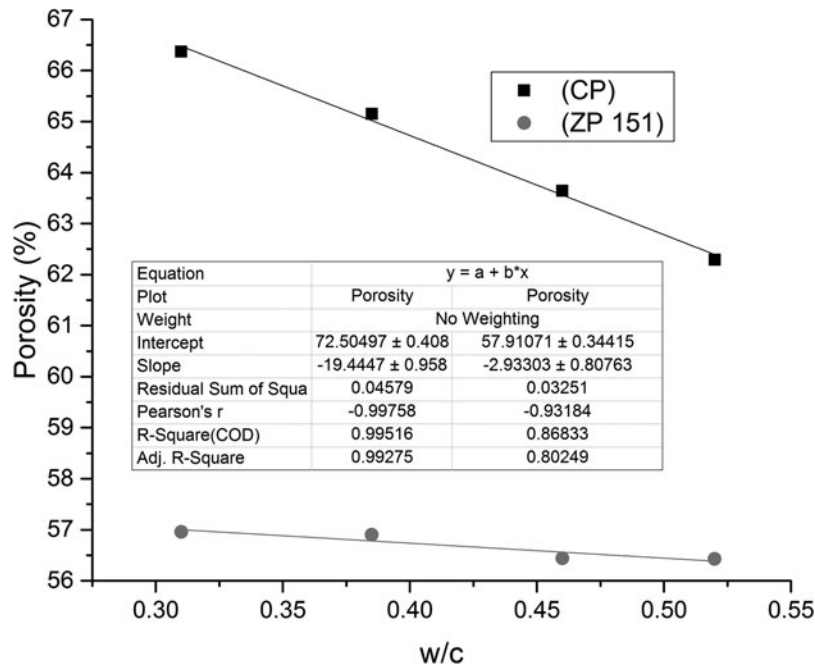


FIG. 25. Linear regression relationship between porosity versus w/c ratio in the 3DP specimen.

strength, 1.61 ± 0.28 MPa, among printed CP specimens. Overall, the 0° orientations demonstrated more acceptable and reliable results in tensile strength for both materials. Thus, it is suggested that the optimal orientation angle to be used in future works is an angle of 0° in the X-direction, printing parallel to the movement of the printhead.

Figure 31 presents the different patterns of dog-bone rupture. A nonuniform rupture can be noticed at the fractured tips of different orientation angles of the dog-bone specimens.

It is obvious the rupture occurred in the lower portion of the specimens, and while the printing orientation angle is smaller. The rupture occurred in a lower section of the printed part due to the high quantity of powder that settled on the lower portion of this section (Fig. 31), which subsequently leads to a weakening in the narrow section of the dog-bone specimens.

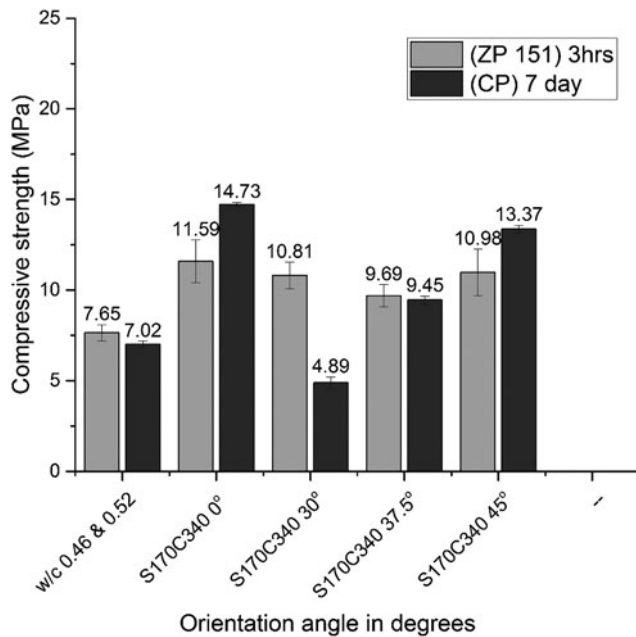


FIG. 26. The compressive strength for the ZP 151 cubes and CP cubes (average ± standard deviation) at saturation level S170C340 in different angles.

Three-point bending test. Three-point bending tests have been conducted to evaluate the flexural strength of the printed ZP 151 and CP (167 × 17 × 7) mm specimens. Figure 32 shows that, in general, the flexural strength in gypsum is higher than the cement mortar specimens. According to ACI330R-01,⁷⁷ the flexural strength of concrete is about 10–20% of the compressive strength result. Likewise, the result of CP in flexural strength tests after 7 days shows that the measured flexural strength is about 14% of the compressive strength. However, this could be due to various factors, including the medium of the specimens, type, sizes, volume of the particle size, and duration of the curing.

Figure 32 shows flexural strength results, which are basically the opposite of the compressive strength results for both materials. As shown in Figure 26, the highest result is in the CP specimens. However, in Figure 32, the results of the ZP 151 show higher values than the CP specimens. Previous studies have proved that using gypsum leads to an increase in bending and tensile strength.⁷⁸ The high percentage of lime content in fly ash with a high ratio of gypsum (1%) leads to a dramatic increase in the tensile strength.⁷⁸ Therefore, gypsum is acting as a flexible material compared to the cement materials. In an earlier study by Lewry and Williamson,⁷⁹ it was proven that the reaction of water to plaster (gypsum), which is similar to the material ZP 151, with a 0.6 w/c ratio could gain about 12.2 MPa of flexural strength. This result is similar to the result for the manual mix of ZP 151 with a w/c ratio of 0.46 that has been presented in this study, which is

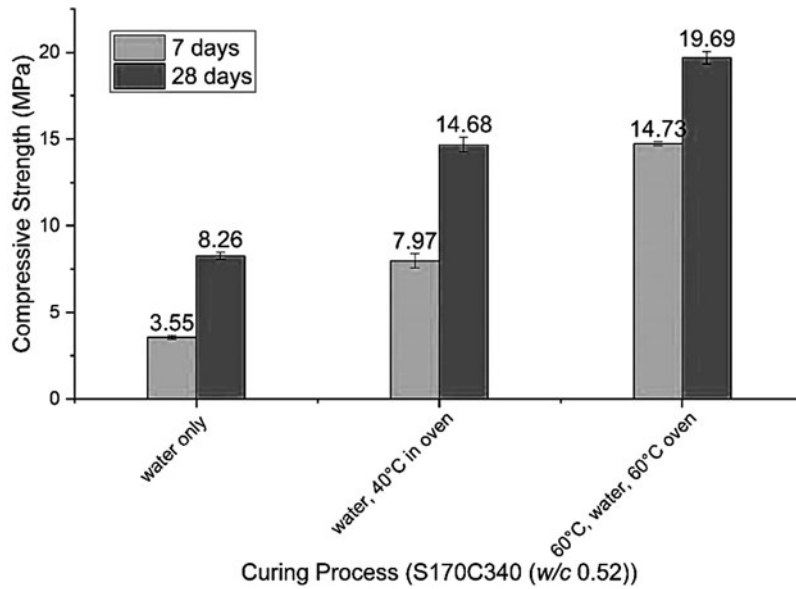


FIG. 27. The compressive strength results for the different curing process, all results are for a printed part (20×20×20) mm in the angle (0°) of the XZ-plane only.

14.23 MPa. However, postprocessing and purity of the materials have a significant effect on the result of the bending strength of gypsum materials.

The highest bending strength result for the printed ZP 151 and CP specimens has been recorded at the orientation angle of 0°. Meanwhile, the manual mix of CP in bending strength is slightly higher than the printed angle 0°. Therefore, in this study when printing with CP, 0° and 90° are the optimum angles to print in for construction members due to the higher results achieved for compressive strength at angle 90° and the higher results achieved for bending strength at angle 0°. It is

hypothesized that the results could be improved further by adding reinforcement, which would make it ideal for use in the façade and cladding of a building.⁸⁰

Orientation angle surface display. The 3D printed mortar specimen is not only different in mechanical properties from traditional mortar but also different in appearance. Figure 33 displays the surface of the cubic cement mortar (CP) in different orientation angles. The photo has been captured by both the 3D microscope scanners: (Olympus LEXT OLS5000) and (Nikon iNEXIV). The photos have been taken in low magnifications to show the printed line for each of the different orientation angles in the CP using (1) the Olympus scanner set at the lowest magnification (5×) and with a working distance of 20 mm, and (2) the Nikon set at the lowest magnification (3.5×) and with a working distance of 73.5 mm. In the images, the printed line of the orientation angles is clearly visible. The image is taken by a different scanner to show the inclined line on the printed surface. Therefore, Olympus and Nikon scanners have been used. The scan by Nikon has a darker feature and could observe the printed line on the surface of the specimen easily. However, the inclined printed parts, specifically 30° and 37.5°, have many visible valleys and a higher roughness compared to the other parts. Therefore, in some images, the blur appeared in angle 30° and 37.5° due to the abundance of uneven surfaces on the mortar specimens (CP). The surface roughness (Ra) of the CP specimen varies in every orientation angle (0°, 30°, 37.5°, 45°, and 90°) and is recorded as 22.3, 25.3, 27.1, 24.3, and 23.1 μm, respectively.

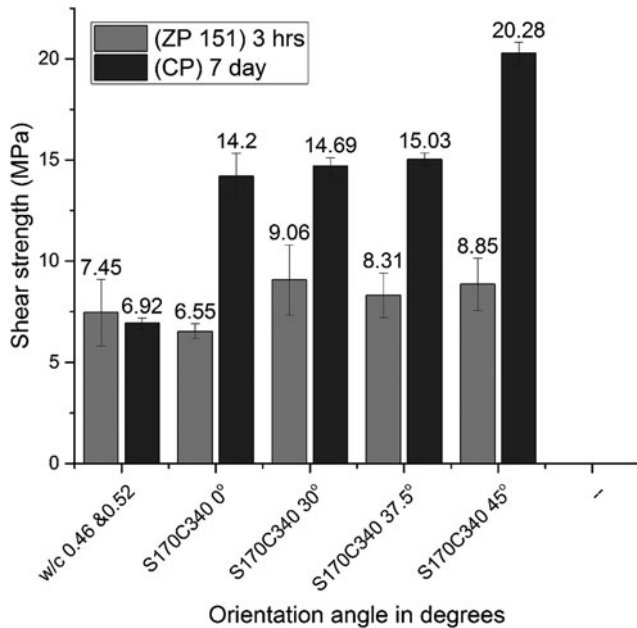


FIG. 28. The shear strength for the CP and ZP 151 cubes (average±standard deviation) at a saturation level of S170C340 for the different orientation angles.

Future work in 3DP using concrete or mortar needs to focus on printing large objects using different techniques such as extrusion and robocasting, which are regularly employed in other manufacturing fields. Extrusion printing can develop rapidly and could produce a strong and smart structure. Such techniques are predicted to be appropriate for use in seismic zones due to the relatively lightweight nature

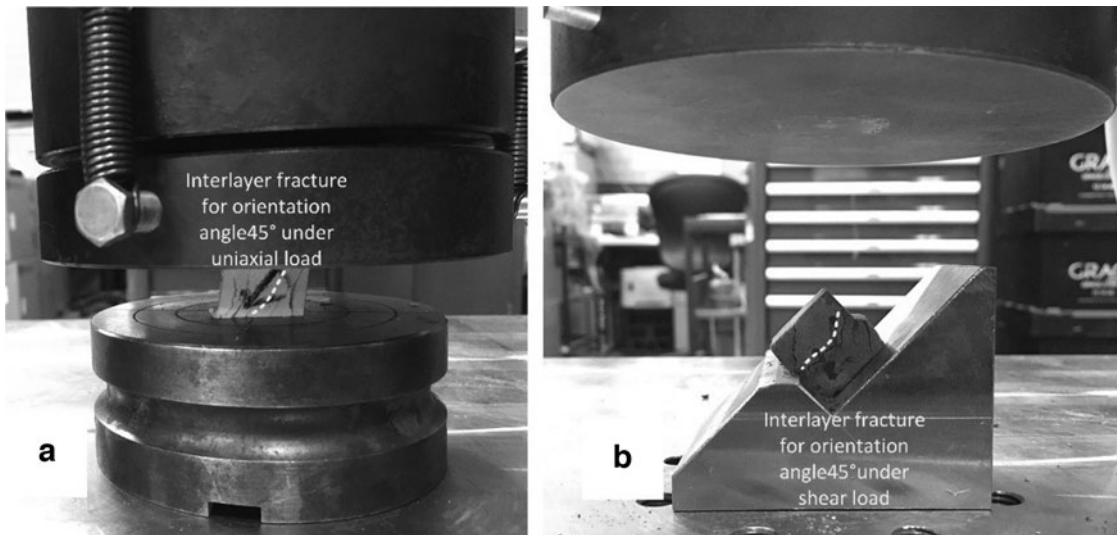


FIG. 29. Fractures in the printed 45° specimens in both (a) compressive test for ZP 151 and (b) shear test for CP.

of the 3DP parts. Based on previous work, it is possible to develop theoretical models to improve the design of structural members with desirable characteristics that can be used for different applications in construction, such as for seismic zones and to reduce the risk of cyclic loading.^{81,82} Therefore, it is expected that the powder bed 3DP could be one of the favorable technologies to be used in construction applications and practices.

Conclusions

3DP technology is emerging as an advanced technique to construct highly detailed complicated structures, which are

conventionally difficult to construct. Based on the experimental investigations, the conclusions can be drawn as follows:

- The effectiveness of the specimen size has been revealed by conducting compressive strength tests on two sets of cubic specimens. Compressive strength experiments in 50×50 mm have a higher result by 11%.
- The effects of heat curing on the different size and with/without glass fiber of the printed mortar specimens were presented. In addition, the maximum compressive strength and flexural strength were recorded at 80°C in the presence of 1% E6-glass fiber.

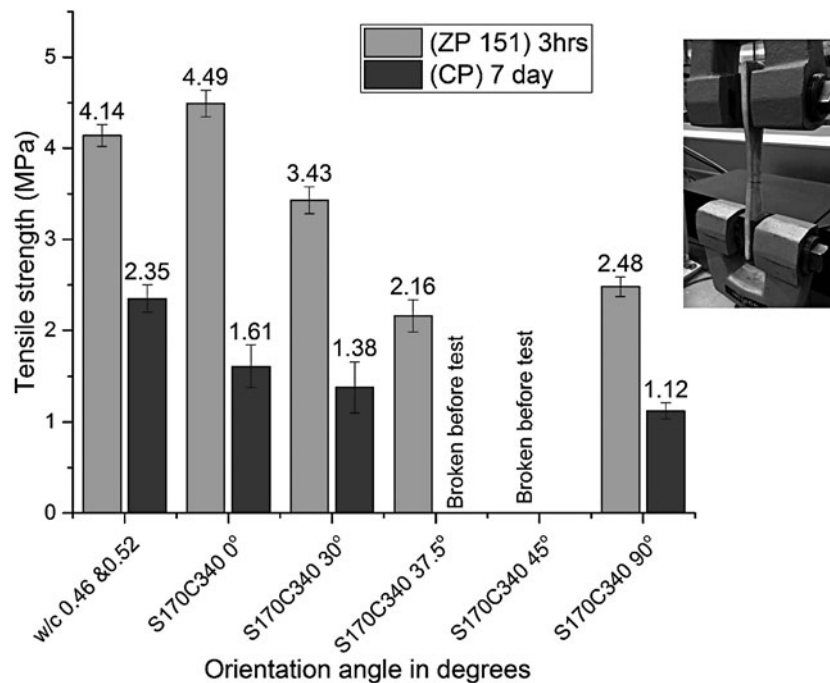


FIG. 30. The tensile strength results for the CP and ZP 151 specimens (average ± standard deviation) at saturation level S170C340 in different orientation angles.

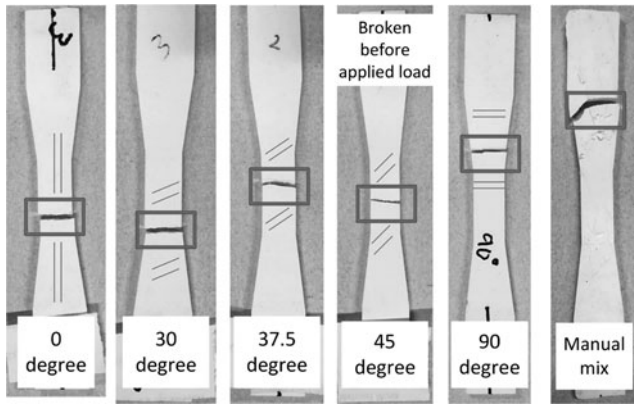


FIG. 31. Cracking present at the dog-bone specimens for the ZP 151 at a different orientation angle.

- It has been discovered that the XY plane (parallel to the applied load), where the load was applied to the face of the YZ plane, showed the maximum mechanical strength. Adding 1% of glass fiber in cubes 50×50 mm increased compressive strength by 58%.
- The surface roughness of the powder bed in the 3DP build chamber for CP and ZP 151 was investigated. The results showed that ZP 151 has an even surface and uniformly distributed particles on the chamber and printed specimen. In printed specimen, the percentage differences between ZP 151 and CP were 47%. When the printed CP specimens (with and

without glass fiber) were scanned, the smoother surface was found in the CP specimen with glass fiber by a difference of 18%.

- The fiber orientation on the build chamber of the printer and fiber filaments in the printed objects were studied and presented, which showed more than 70% spread parallel to Y-axis.
- Effectiveness of binder (water) dosage was discussed with the indication of binder droplet penetration on the CP and ZP 151 powder: the diameter of the binder on the CP surface 10% larger than ZP 151 and the depth of the binder in CP powder 12% shallower than ZP 151.
- The maximum deflection recorded during the tensile strength tests of the printed part for the ZP 151 and CP specimens was at 45° (rotation to XZ-plane) due to the maximum incline position of the specimens and the maximum unbounded powder on the specimen, which was loaded on the specimens in the build chamber.
- The most suitable orientations and the strongest angles have been discovered to be at 0° for both flexural and compression strength tests for CP and ZP 151. For CP specimens, the maximum shear strength has been recorded at 45° and the maximum tensile strength was recorded at 0°.

It is recommended that further research on powder-based 3DP is required, specifically on the postprocessing, curing, and infiltration, and early age shrinkage of the printed specimens such as autogenous shrinkage, chemical shrinkage, and

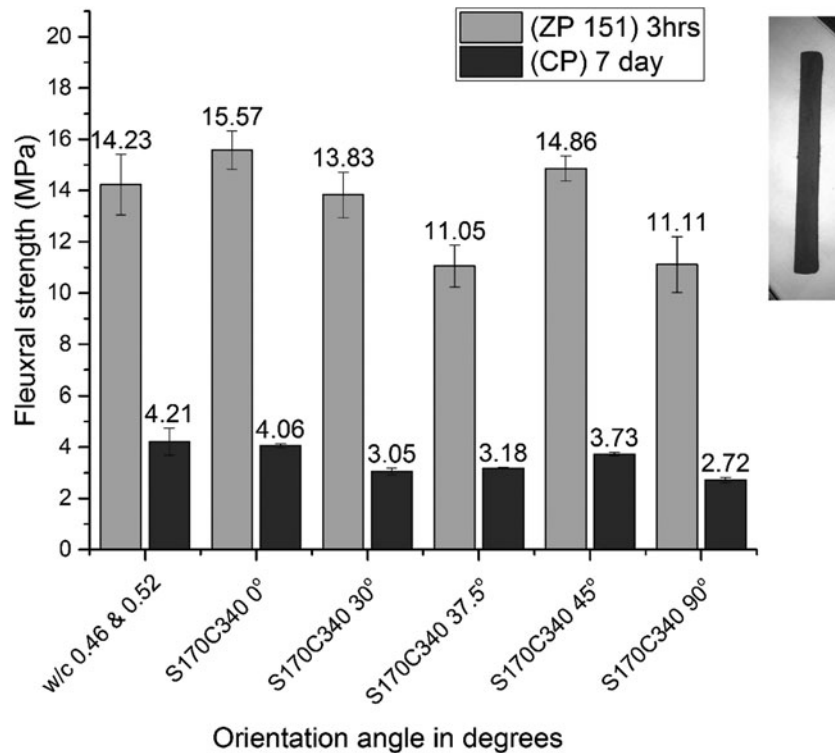


FIG. 32. The flexural strength results for the ZP 151 specimens and CP specimens (average ± standard deviation) at saturation level S170C340 in different angles.

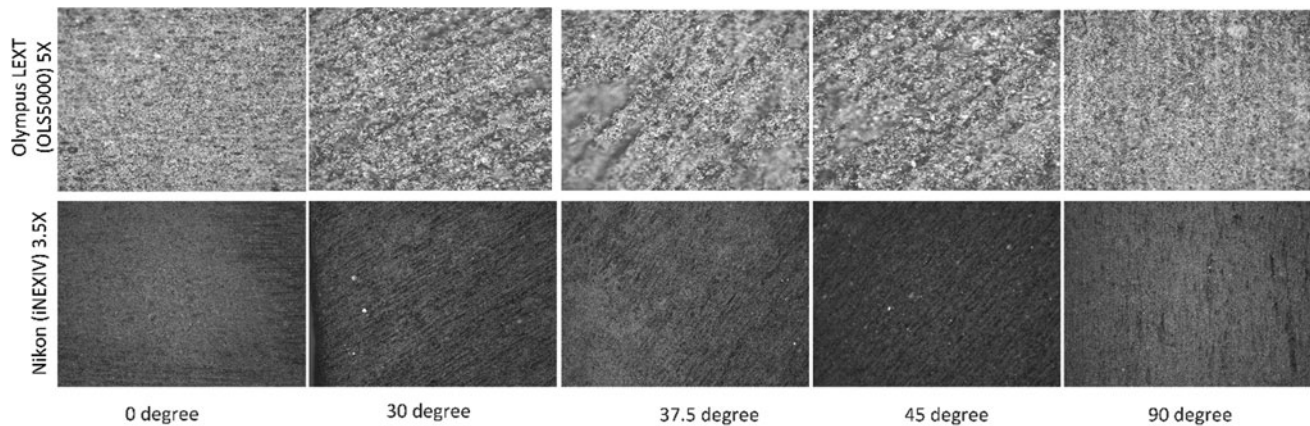


FIG. 33. Surface images of the cubic specimens of CP at orientation angles of (0° , 30° , 37.5° , 45° , and 90°) by the Nikon and Olympus 3D laser microscopes.

plastic settlement shrinkage. Preferably, research will focus on the broader applications for construction purposes, such as an investigation of larger-scale prints in real life.

Acknowledgments

The authors are thankful for the support of the Civil Engineering Laboratory at the University of Technology Sydney. The authors would like to acknowledge the Environmental Science lab and Metrology lab for their help and for allowing the authors to utilize their facilities. Finally, the authors would like to express their appreciation to Kerneos Australia Pty Limited for providing the CAC.

Author Disclosure Statement

No competing financial interest exists.

Funding Information

No funding was received for this work.

References

- Haroglu H. Investigating the Structural Frame Decision Making Process. Loughborough University: United Kingdom, 2010.
- Nerella VN, Mechtcherine V. *Chapter 16-Studying the Printability of Fresh Concrete for Formwork-Free Concrete Onsite 3D Printing Technology (CONPrint3D)*, in *3D Concrete Printing Technology*, In: Sanjayan JG, Nazari A, Nematollahi B, (eds.) *3D Concrete Printing Technology*, Butterworth-Heinemann, 2019, pp. 333–347.
- Chu SH, Li LG, Kwan AKH. Development of extrudable high strength fiber reinforced concrete incorporating nano calcium carbonate. *Addit Manuf* 2021;37:101617.
- ASTM:F2792-12a. American Society of Testing and Materials (withdrawn). 2012.
- Kazemian A, Yuan X, Cochran E, Khoshnevis B, *et al.* Cementitious materials for construction-scale 3D printing: laboratory testing of fresh printing mixture. *Construct Build Mater* 2017;145:639–647.
- Lloret E, Shahab AR, Linus M, *et al.* Complex concrete structures: merging existing casting techniques with digital fabrication. *Comput Aided Des* 2015;60:40–49.
- Perrot A, Rangeard D, Pierre A. Structural built-up of cement-based materials used for 3D-printing extrusion techniques. *Mater Struct* 2015;49:1213–1220.
- Lee J-Y, An J, Chua CK. Fundamentals and applications of 3D printing for novel materials. *Appl Mater Today* 2017; 7:120–133.
- Yang H, Lim JC, Liu Y, *et al.* Performance evaluation of ProJet multi-material jetting 3D printer. *Virtual Phys Prototyp* 2017;12:95–103.
- Joocho M, Grau JE, Knezevic V, *et al.* Ink-jet printing of binders for ceramic components. *J Am Ceram Soc* 2002;85:755.
- 3D Systems. ZPrinter 150/ZPrinter 250 Overview. 2012. http://infocenter.3dsystems.com/product-library/sites/default/files/printers/Z_Printer/Z150_250/95008%20ZPrinter%20150%20and%20250%20User%20Manual.pdf (last accessed December 11, 2019).
- Majeed SA. Effect of specimen size on compressive, modulus of rupture and split-tensile strength of cement mortar. *J Appl Sci* 2011;11:584–588.
- Dizon JRC, *et al.* *Mechanical characterization of 3D-printed polymers*. *Addit Manuf* 2018;20:44–67.
- Pena F. The role of the tension strength in the collapse mechanism of unreinforced brick masonry constructions. In: 13th World Conference on Earthquake Engineering, Vancouver, B.C., Canada, 2004.
- Feng P, Meng X, Chen J-F, *et al.* Mechanical properties of structures 3D printed with cementitious powders. *Construct Build Mater* 2015;93:486–497.
- Torrado AR, Shemelya CM, English JD, *et al.* Characterizing the effect of additives to ABS on the mechanical property anisotropy of specimens fabricated by material extrusion 3D printing. *Addit Manuf* 2015;6:16–29.
- Lowke D, Dini E, Perrot A, *et al.* Particle-bed 3D printing in concrete construction—possibilities and challenges. *Cement Concrete Res* 2018;112:50–65.
- Farina I, Fabbrocino F, Colangelo F, *et al.* Surface roughness effects on the reinforcement of cement mortars through 3D printed metallic fibers. *Compos B Eng* 2016;99:305–311.
- Zhou Z, Buchanan F, Mitchell C, *et al.* Printability of calcium phosphate: calcium sulfate powders for the application of tissue engineered bone scaffolds using the 3D printing technique. *Mater Sci Eng C Mater Biol Appl* 2014;38:1–10.
- Shanjani Y, Toyserkani E. Material spreading and compaction in powder-based solid freeform fabrication

- methods: mathematical modeling. In: 19th Annual International Solid Freeform Fabrication Symposium, SFF, University of Texas, Austin, USA, 2008.
21. Falliano D, De Domenico D, Ricciardi G, *et al.* Improving the flexural capacity of extrudable foamed concrete with glass-fiber bi-directional grid reinforcement: an experimental study. *Compos Struct* 2019;209:45–59.
 22. Kodur V. Properties of concrete at elevated temperatures. *ISRN Civil Eng* 2014;2014:468510.
 23. Sanjayan G, Stocks L. Spalling of high-strength silica fume concrete in fire. *Mater J* 1993;90:170–173.
 24. Li VC, Maalej M. Toughening in cement based composites. Part II: fiber reinforced cementitious composites. *Cement Concr Compos* 1996;18:239–249.
 25. Feng P, Meng X, Zhang H. Mechanical behavior of FRP sheets reinforced 3D elements printed with cementitious materials. *Compos Struct* 2015;134:331–342.
 26. Christ S, Schnabel M, Vorndran E, *et al.* Fiber reinforcement during 3D printing. *Mater Lett* 2015;139:165–168.
 27. Farina I, Fabbrocino F, Carpentieri G, *et al.* On the reinforcement of cement mortars through 3D printed polymeric and metallic fibers. *Compos B Eng* 2016;90:76–85.
 28. Panda B, Paul SC, Tan MJ. Anisotropic mechanical performance of 3D printed fiber reinforced sustainable construction material. *Mater Lett* 2017;209:146–149.
 29. Farzadi A, Solati-Hashjin M, Asadi-Eydivand M, *et al.* Effect of layer thickness and printing orientation on mechanical properties and dimensional accuracy of 3D printed porous samples for bone tissue engineering. *PLoS One* 2014;9:e108252.
 30. Dizon JRC, Espera AH, Chen Q, *et al.* Mechanical characterization of 3D-printed polymers. *Addit Manuf* 2018; 20:44–67.
 31. Letcher T, Waytashek M. Material property testing of 3D-printed specimen in PLA on an entry-level 3D printer. In: ASME 2014 International Mechanical Engineering Congress and Exposition, American Society of Mechanical Engineers, Montreal, Quebec, Canada, 2014.
 32. Coelho AWF, da Silva Moreira Thiré RM, Araujo AC. Manufacturing of gypsum–sisal fiber composites using binder jetting. *Addit Manuf* 2019;29:100789.
 33. Shakor P, Gowripalan N, Rasouli H. Experimental and numerical analysis of 3D printed cement mortar specimens using inkjet 3DP. *Arch Civil Mech Eng* 2021;21:58.
 34. 3D Systems. ZP151 Powder Safety Data Sheet. 2013. http://infocenter.3dsystems.com/materials/sites/default/files/sds-files/legacy/powders/ZP151/2548_360201-S12-02-A,SDS%20GHS,English,zp151.pdf (last accessed December 11, 2019).
 35. Shakor P, Nejadi S, Paul G, *et al.* Mechanical properties of cement-based materials and effect of elevated temperature on three-dimensional (3-D) printed mortar specimens in inkjet 3-D printing. *ACI Mater J* 2019; 116:55–67.
 36. Zhang H, Zhao H, Chen J, *et al.* Defect study of MgO–CaO material doped with CeO₂. *Adv Mater Sci Eng* 2013; 2013:5.
 37. Hill J, Orr J, Dunne N. In vitro study investigating the mechanical properties of acrylic bone cement containing calcium carbonate nanoparticles. *J Mater Sci Mater Med* 2008;19:3327–3333.
 38. 3D Systems. ZB63 Safety Data Sheet. 2012. http://infocenter.3dsystems.com/materials/sites/default/files/sds-files/legacy/binders/ZB63/2548_50423-S12-01-A%2CGHS%2CEnglish-Australia%2Czb63.pdf (last accessed December 11, 2019).
 39. Shakor P, Nejadi S, Paul G, *et al.* Dimensional accuracy, flowability, wettability, and porosity in inkjet 3DP for gypsum and cement mortar materials. *Autom Construct* 2020;110:102964.
 40. ASTM C39. 39, Standard Test Method for Compressive Strength of Cylindrical Concrete Specimens. ASTM International, 2001.
 41. ASTM C293/C293M. 293 Standard Test Method for Flexural Strength of Concrete (Using Simple Beam with Center-Point Loading). ASTM Standard 2002.
 42. Cao RH, Cao P, Lin H, *et al.* Failure characteristics of jointed rock-like material containing multi-joints under a compressive-shear test: experimental and numerical analyses. *Arch Civil Mech Eng* 2018;18:784–798.
 43. ASTM D638. Standard Test Method for Tensile Properties of Plastics. 2014.
 44. Lothenbach B, Winnefeld F, Alder C, *et al.* Effect of temperature on the pore solution, microstructure and hydration products of Portland cement pastes. *Cement Concrete Res* 2007;37:483–491.
 45. Abd elaty MAA. Compressive strength prediction of Portland cement concrete with age using a new model. *HBRC J* 2014;10:145–155.
 46. Amin MN, Khan K, Saleem MU, *et al.* Aging and curing temperature effects on compressive strength of mortar containing lime stone quarry dust and industrial granite sludge. *Materials* 2017;10:642.
 47. Altan E, Erdoğan ST. Alkali activation of a slag at ambient and elevated temperatures. *Cement Concr Compos* 2012; 34:131–139.
 48. Bellego CL, Gérard B, Pijaudier-Cabot G. Chemo-mechanical effects in mortar beams subjected to water hydrolysis. *J Eng Mech* 2000;126:266–272.
 49. Sagoe-Crentsil K, Weng L. Dissolution processes, hydrolysis and condensation reactions during geopolymer synthesis: part II. High Si/Al ratio systems. *J Mater Sci* 2007; 42:3007–3014.
 50. Abdulkareem OA, Mustafa Al Bakri AM, Kamarudin H, *et al.* Effects of elevated temperatures on the thermal behavior and mechanical performance of fly ash geopolymer paste, mortar and lightweight concrete. *Construct Build Mater* 2014;50:377–387.
 51. Chen Y, Liang C, Wang X, *et al.* Static pressure distribution characteristics of powders stored in silos. *Chem Eng Res Des* 2020;154:1–10.
 52. Beverloo WA, Leniger HA, Van de Velde J. The flow of granular solids through orifices. *Chem Eng Sci* 1961; 15:260–269.
 53. Graybeal B, Davis M. Cylinder or cube: strength testing of 80 to 200 MPa (11.6 to 29 ksi) ultra-high-performance fiber-reinforced concrete. *ACI Mater J* 2008;105:603–609.
 54. An M-Z, Zhang L-J, Yi Q-X. Size effect on compressive strength of reactive powder concrete. *J China Univ Mining Technol* 2008;18:279–282.
 55. Dehestani M, Nikbin IM, Asadollahi S. Effects of specimen shape and size on the compressive strength of self-consolidating concrete (SCC). *Construct Build Mater* 2014; 66:685–691.
 56. del Viso JR, Carmona JR, Ruiz G. Shape and size effects on the compressive strength of high-strength concrete. *Cement Concrete Res* 2008;38:386–395.

57. Yi S-T, Yang E-I, Choi J-C. Effect of specimen sizes, specimen shapes, and placement directions on compressive strength of concrete. *Nucl Eng Des* 2006;236:115–127.
58. Tokyay M, Özdemir M. Specimen shape and size effect on the compressive strength of higher strength concrete. *Cement Concrete Res* 1997;27:1281–1289.
59. Zabihi N, Eren Ö. Compressive strength conversion factors of concrete as affected by specimen shape and size. *Res J Appl Sci Eng Technol* 2014;7:4251–4257.
60. Fládr J, Bílý P. Specimen size effect on compressive and flexural strength of high-strength fibre-reinforced concrete containing coarse aggregate. *Compos B Eng* 2018;138:77–86.
61. Shakor P, Sanjayan J, Nazari A, *et al.* Modified 3D printed powder to cement-based material and mechanical properties of cement scaffold used in 3D printing. *Construct Build Mater* 2017;138:398–409.
62. Castilho M, Dias M, Gbureck U, *et al.* Fabrication of computationally designed scaffolds by low temperature 3D printing. *Biofabrication* 2013;5:035012.
63. Petzing JN, Coupland JM, Leach RK. 2010. The measurement of rough surface topography using coherence scanning interferometry. Loughborough University. Report. <https://hdl.handle.net/2134/13271> (last accessed May 7, 2017).
64. Shakor P, Nejadi S, Gowripalan N. Effect of Heat Curing and E6-Glass Fibre Reinforcement Addition on Powder-Based 3DP Cement Mortar. Cham: Springer International Publishing, 2020.
65. JushiUSA. Chopped strands 552B for BMC. <http://jushiusa.com/content/chopped-strands-552b> (last accessed January 4, 2019).
66. Zortuk M, Kilic K, Uzun G, *et al.* The effect of different fiber concentrations on the surface roughness of provisional crown and fixed partial denture resin. *Eur J Dent* 2008; 2:185–190.
67. Kahlin M, Ansell H, Basu D, *et al.* Improved fatigue strength of additively manufactured Ti6Al4V by surface post processing. *Int J Fatigue* 2020;134:105497.
68. Júlio ENBS, Branco FAB, Silva VTD. Concrete-to-concrete bond strength. Influence of the roughness of the substrate surface. *Construct Build Mater* 2004;18: 675–681.
69. Alhumdany A, Abidali A, Abdulredha H. Investigation of wear behaviour for NiTi alloys with yttrium and tantalum additions. *IOP Conf Ser Mater Sci Eng* 2018;433:012072.
70. Bredt JF, Anderson TC, Russell DB. Three dimensional printing material system and method. Google Patents, 2003.
71. Popovics S, Ujhelyi J. Contribution to the concrete strength versus water-cement ratio relationship. *J Mater Civil Eng* 2008;20:459–463.
72. ACI308R-01. Standard Guide to Curing Concrete. 2001. https://www.techstreet.com/standards/aci-308r-01?product_id=726 (last accessed February 21, 2018).
73. Asadi-Eydivand M, Solati-Hashjin M, Farzad A, *et al.* Effect of technical parameters on porous structure and strength of 3D printed calcium sulfate prototypes. *Robot Comput Integr Manuf* 2016;37:57–67.
74. Dias WPS. Reduction of concrete sorptivity with age through carbonation. *Cement Concrete Res* 2000;30:1255–1261.
75. Parrott LJ. Moisture conditioning and transport properties of concrete test specimens. *Mater Struct* 1994;27:460.
76. Sarangapani G, Venkatarama Reddy B, Jagadish K. Brick-mortar bond and masonry compressive strength. *J Mater Civil Eng* 2005;17:229–237.
77. ACI Committee. ACI330R-01. Guide for Design and Construction of Concrete Parking Lots. 2001. http://www.wef-pe.com/downloads/ACI-330_Design_Guide_for_Concrete_Parking_Lots%5B1%5D.pdf (last accessed February 21, 2018).
78. Ghosh A, Subbarao C. Tensile strength bearing ratio and slake durability of class F fly ash stabilized with lime and gypsum. *J Mater Civil Eng* 2006;18:18–27.
79. Lewry AJ, Williamson J. The setting of gypsum plaster. *J Mater Sci* 1994;29:6085–6090.
80. Enfedaque A, Cendón D, Gálvez F, *et al.* Failure and impact behavior of facade panels made of glass fiber reinforced cement (GRC). *Engineering Failure Analysis* 2011;18:1652–1663.
81. Sonebi M, Amziane S, Perrot A. Mechanical behavior of 3D printed cement materials. In *3D Printing of Concrete: State of the Art and Challenges of the Digital Construction Revolution*. 2019. Wiley-ISTE. <https://doi.org/10.1002/9781119610755>.
82. Cheok G, Stone W, Kunnath S. Seismic response of precast concrete frames with hybrid connections. *Struct J* 1998; 95:527–539.

Address correspondence to:

Pshtiwan Shakor
School of Civil and Environmental Engineering
University of Technology Sydney
Ultimo
NSW 2007
Australia

E-mail: pshtiwan.shakor@uts.edu.au